Selection of Reconstruction Parameters

David Long, BYU
Draft 3.3
16 Mar 2015

Abstract

This report reviews the theory of radiometer image formation and reconstruction. It presents simulation results used to select the nominal pixel size and reconstruction algorithms for the Calibrated Passive Microwave Daily EASE-Grid 2.0 Brightness Temperature ESDR (CETB). Two primary reconstruction algorithms are considered, the Backus-Gilbert Interpolation (BGI) approach and the Scatterometer Image Reconstruction (SIR). These are compared to the conventional drop-in-the-bucket gridded image formation algorithms. Tradeoff study results for the various algorithm options are presented, including the grid sizes, the number of SIR iterations, and the BGI gamma parameter, and recommendations for each are provided to the CETB project. The sensitivity of the reconstruction to the accuracy of the measurement spatial response function is also explored.

1.1 Gridding and Reconstruction

All algorithms to transform radiometer data from swath to gridded format are characterized by a tradeoff between noise and spatial resolution. Our intention with the Calibrated Passive Microwave Daily EASE-Grid 2.0 Brightness Temperature ESDR (CETB) project (Brodzik and Long, 2014) is to produce both low-noise gridded data and enhanced-resolution data products. The low resolution gridded data has lower noise, while the high resolution data has potentially higher noise. This will enable product users to compare and choose which option better suits a particular research application. The purpose of this report is to provide background into the theory of each approach with the goal of providing transparency into the tradeoff decisions made in defining the CETB.

In the CETB all radiometer channels will be gridded to the coarsest resolution (25 km) grids using the drop-in-the-bucket method described below. These products are termed ‘low resolution’ or ‘non-enhanced resolution’ and denoted as GRD or Grd products. Higher resolution products are generated using one of two image reconstruction methods, the radiometer form of the Scatterometer Image Reconstruction (SIR) algorithm and the Backus-Gilbert Interpolation or Image formation (BGI) method, as described below. Channels will be gridded at enhanced resolution on nested grids at power of 2 relationships to the base 25 km grid. The method for determining the finest resolution for each channel is given below. Unlike the approach taken for the historical EASE-Grid data (Armstrong, et al., 1994), the CETB will not attempt to match the resolution of the highest channels to the coarsest channel, but will independently optimize the resolution for each channel in the high resolution products.

The image grids for the CETB are Earth-located (in contrast to swath-based) using the EASE-2.0 projection (Brodzik et al., 2012). In generating gridded data, only measurements from a single sensor and channel are processed. Measurements combined into a single grid element may have different Earth azimuth and incidence angles (though the incidence angle variation is small). Measurements from multiple orbit passes over a narrow local time may be combined. When multiple measurements are combined, the resulting images represent an average of the measurements over the averaging period. There is an implicit assumption that the surface characteristics remain constant over the imaging period and that there is no azimuth variation in the true surface brightness temperature (T_B).

For both non-enhanced and enhanced resolution images, the effective gridded image resolution depends on the number of measurements and the precise details of their spatial response functions, including overlap, orientation, and location.

1.2 Theory of Reconstruction and Gridding Algorithms

This section provides a brief summary of the algorithms used for reconstruction and gridding. Gridded data are separately computed for each channel and instrument.

1.2.1 Coarse Resolution (GRD) Gridding Algorithm

The planned CETB coarse resolution gridding procedure is a simple, "drop-in-the-bucket" average. The resulting data grids are designated GRD data arrays. For the drop-in-the-bucket gridding algorithm, the key information required is the location of the measurement. The center of each measurement location is mapped to an output projected grid cell. All measurements within the specified time period whose centers fall within the bounds of a particular grid cell are averaged together. No weighting is done. The measurement is the reported T_B value for this pixel. Ancillary product files contain the number and standard deviation of included samples.

Note that the effective spatial resolution of the GRD product is defined by a combination of the pixel size and spatial extent of the 3dB antenna footprint size (Long and Daum, 1998) and does not require any information about the antenna pattern. While the pixel size can be arbitrarily set, the effective resolution is, to first-order, the sum of the pixel size plus the footprint dimension. All gridded products are produced on a 25 km pixel grid and thus have an effective spatial resolution that is coarser than 25 km.

Here we consider several definitions of the GRD product. The baseline is a standard "drop-in-the-bucker" (DIB) where a measurement is assigned to the rectangular grid element (pixel) in which the measurement center falls. Multiple measurements may be averaged within one pixel, but each measurement is accumulated into a single pixel. In this section, this is referred to as a standard DIB (DIB0). An alternate DIB definition is based on assigning pixels to a measurement based on the measurement being with a particular radius of the pixel center. In this case, a measurement may be averaged into multiple pixels. Here we consider a radius of 1/sqrt(2) of the grid dimension, which corresponds to a minimum sized circle that encloses a single (square) pixel. This is denoted as DIB1. Finally, the value within each pixel can be computed as the weighted average of all “nearby” measurements where “nearby” is defined as measurements within a given radius. The weighting function is the inverse distance squared, denoted IDG1. In IDG1, one measurement is included in multiple measurements.

To simplify later analysis we present a comparison between these conventional gridding algorithms based on simulation results for the SSM/I 37 GHz channel with two passes described later. Simulated measurements are created of a synthetic “truth” image at high resolution using the measurement SRF. Both noisy and noise-free simulation results are considered. The error between the gridded data and the true image is summarized in Table 0. Figure 0 compares the GRD image with the truth image.

Though there is not a lot of visual difference in the images, DIB0 is the visually the least noisy, has the smallest RMS error (see Table 0), and is subjectively sharpest of the three algorithms. The IDG1 is the next best. Since it has the lowest noise and error, in the following only DIB0 is used for the GRD comparison images.

Table 0: Comparison of the errors for different gridding options. To compute the error the gridded image is pixel replicated to the same size/resolution and the true image. The error is the difference between the true image and the pixel-replicated estimated image. The mean, standard deviation (STD), and root-mean-square (RMS) error values are then computed.

Case	Mean err (K)	Err STD (K)	Err RMS (K)
DIB0 Noise-free	-0.02	4.64	4.64
DIB1 Noise-free	-0.11	5.34	5.34
IDG1 Noise-free	-0.09	4.83	4.83
DIB0 Noisy	-0.02	4.73	4.73
DIB1 Noisy	-0.10	5.40	5.40
IDG1 Noisy	-0.09	4.98	4.98

1.2.2 Reconstruction Algorithms

In reconstruction algorithms, the effective measurement response function (MRF) is used. The MRF is determined by the antenna gain pattern (which is unique for each sensor and sensor channel, and may vary with scan angle), the scan geometry (notably the antenna scan angle), and the integration period. The latter “smears” the antenna gain pattern due to antenna rotation over the measurement integration period. The MRF describes how much the emissions from a particular receive direction contribute to the observed TB value.

Denote the MRF for a particular channel by $R(\varphi,\theta;\ \phi)$ where φ and θ are particular azimuth and elevation angles relative to the antenna boresite at a scan angle ϕ (ϕ *is* sometimes referred to as the antenna azimuth angle). Note that for a given antenna azimuth scan angle the integral of the MRF R over all azimuth and elevation angles is 1.

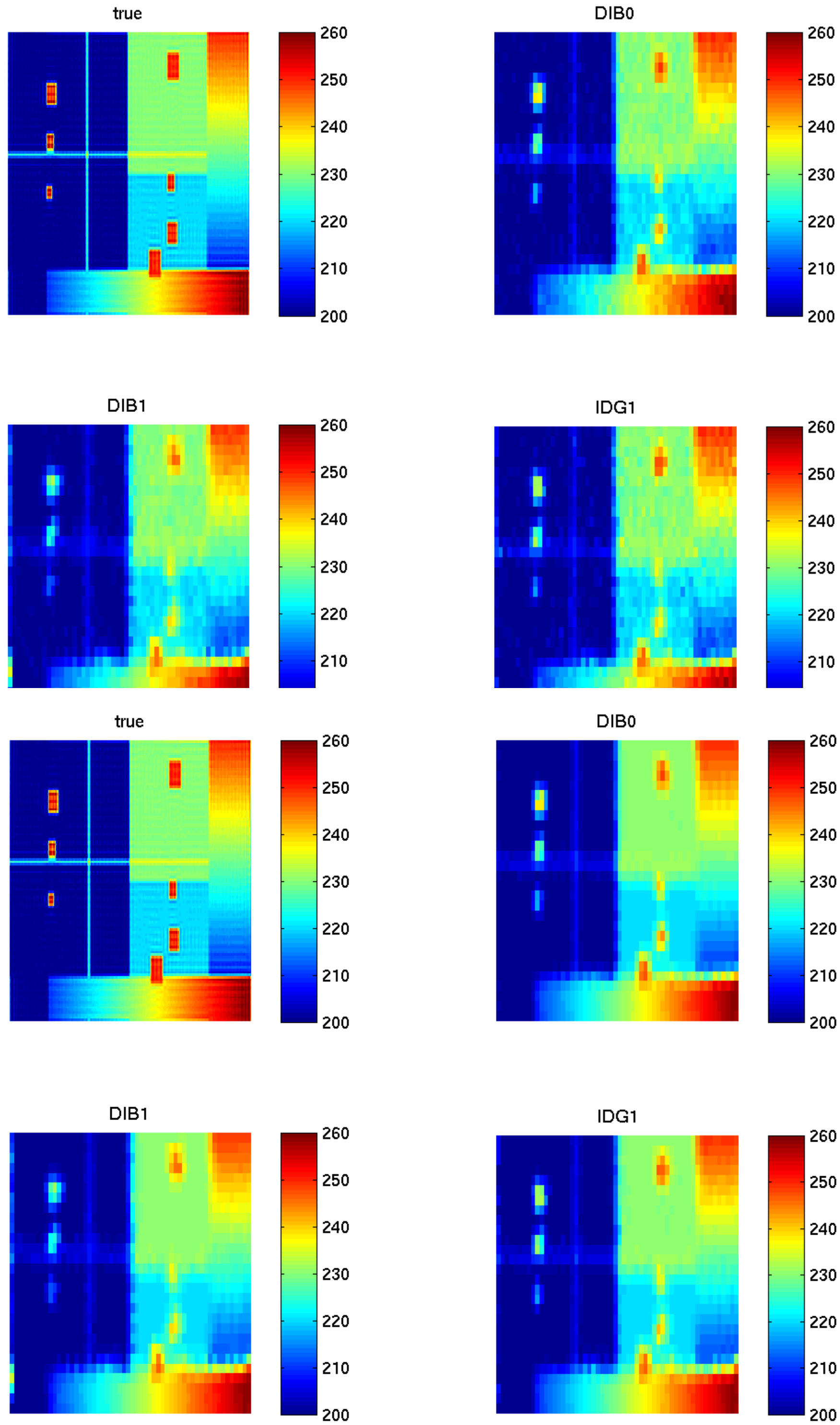

Figure 0. Comparison of DIB gridding algorithm results. Top 4 panels are noisy, while bottom 4 are noise-free. (Truth is noise-free.)

Generally, for the Fundamental Climate Data Record (FCDR) data sets that are input to the CETB, the MRF can be treated as zero everywhere but in the direction of the surface. With this assumption, we can write $R(\varphi,\theta;\ \phi)$ as $R(x,y;\ \phi)$ where x and y are the location (which we will express in map coordinates) on the surface corresponding to the azimuth and elevation angles. Note that:

$$\iint_{surface} R(x,y;\phi_i)dxdy = 1$$

Equation 1

Then, a particular measurement T_i can be written as

$$T_i = \iint_{surface} R(x,y;\phi_i)T_B(x,y;\phi_i)dxdy$$

Equation 2

where the scan angle ϕ_i corresponds to the scan angle at the center (or start) of the integration period and $T_B(x,y;\ \phi_i)$ is the nominal brightness temperature in the direction of point x,y on the surface as observed from the scan angle position. Note that if there is no significant difference in the atmospheric contribution as seen from different scan angles, we can treat $T_B(x,y;\ \phi_i)$ as independent of ϕ_i so that $T_B(x,y;\ \phi_i)=T_B(x,y)$. For convenience $T_B(x,y)$ is referred to as the surface brightness temperature.

With this approximation, we can write Equation 2 as,

$$T_i = \iint_{surface} R(x,y;\phi_i)T_B(x,y)dxdy$$

Equation 3

Each measurement is seen to be the MRF-weighted average of *TB*. The goal of the reconstruction algorithm is to estimate $T_B(x,y)$ from the measurements T_i.

In the following, two approaches (Long and Daum, 1998) to inferring the surface brightness temperature are presented. The first is based on signal processing, and treats the surface brightness temperature as a two-dimensional signal to be estimated from irregular samples (the measurements). The second is a least-squares approach to signal estimation based on the Backus and Gilbert (1967) approach.

Both approaches enable estimation of the surface brightness on a finer grid than possible with the gridded approach, i.e., the resulting brightness temperature estimate has a finer effective spatial resolution than the gridded approach. As a result, the results are often called "enhanced resolution," though in fact, reconstruction algorithms merely exploit the available information to reconstruct the original signal at higher resolution than gridding under the assumption of a bandlimited signal (Early and Long, 2001). The resolution enhancement possible compared to a gridded product depends on the sampling density and the MRF; however, improvements in the effective resolution of 25% to 1000% have been demonstrated in practice for particular applications. For radiometer enhancement, the effective improvement in resolution tends to be limited, and in practice is typically less than 100% improvement. Note that in order to meet Nyquist requirements for the signal processing, the pixel resolution of the images must be finer than the effective resolution by at least a factor of two.

For comparison, note that the effective resolution for drop-in-the bucket gridding is defined as the grid size plus the spatial dimension of the measurement, which is typically defined by the half-power or the 3 dB beamwidth. Based on Nyquist considerations, the highest representable frequency for drop-in-the bucket gridding is twice the grid spacing.

In the polar regions, multiple passes over the same area are frequently averaged together. Reconstruction algorithms intrinsically exploit the resulting oversampling of the surface to improve the effective spatial resolution in the final image.

1.3 Signal Reconstruction

In the reconstruction/signal processing approach, $T_B(x,y)$ is treated as a noisy two-dimensional signal to be estimated from the measurements T_i. For practical reasons, $T_B(x,y)$ is treated as a discrete signal sampled at the map pixel spacing. This spacing must be set sufficiently fine so that the generalized sampling requirements (Gröchenig, 1992) are met for the signal and the measurements (Early and Long, 2001). Typically, this is one-fourth to one-tenth the size of antenna footprint size. The CETB product is produced at this fine resolution even though the effective resolution of the enhanced resolution images is coarser than the pixel dimension.

Let $T_B[x,y]$ be the discretely sampled surface brightness temperature we are attempting to estimate. To briefly describe the theory, for convenience we vectorize this two-dimensional signal over an N_x by N_y pixel grid into a single dimensional variable a_j where

$$a_j = T_B[x_l, y_k]$$

Equation 4

with $j=l+N_x k$ The measurement equation, Equation 3, becomes

$$T_i = \sum_{j \in image} h_{ij} a_j$$

Equation 5

where $h_{ij} = R(x_l, y_k;\ \phi_i)$ is the discrete MRF for the ith measurement evaluated at the jth pixel center and the summation is over the image. We require that the discrete MRF be normalized so that

$$1 = \sum_{j \in image} h_{ij}$$

Equation 6

In practice, the MRF is negligible some distance from the measurement so this sum need only be computed over an area local to the measurement position. Some care has to be taken near image boundaries.

For the collection of available measurements, Equation 5 can be written as the matrix equation

$$\vec{T} = \mathbf{H}\vec{a}$$

Equation 7

where **H** contains the sampled MRF for each measurement. Note that **H** is (very) large, sparse, and may be overdetermined or underdetermined.

Estimating the brightness temperature at high resolution is equivalent to inverting Equation 7. While a variety of approaches to this have been proposed, in practice, due to the large size of **H**, iterative methods are used. One advantage of an iterative method is that regularization can be easily implemented by prematurely terminating the iteration; otherwise an explicit regularization method can be used.

The radiometer form of the Scatterometer Image Reconstruction (SIR) is a particular implementation of an iterative solution to Equation 7 that has proven effective in generating high resolution brightness temperature images (Long and Daum, 1998). The SIR estimate approximates a maximum-entropy solution to an underdetermined equation and least-squares to an overdetermined system. SIR can provide results similar to the Backus/Gilbert method described below, but with significantly less computation. The first iteration of SIR is termed AVE, and can be a useful estimate of the surface T_B of its own. The AVE estimate of the jth pixel is given by

$$a_j = \frac{\sum h_{ij} T_i}{\sum h_{ij}}$$

Equation 8

where the sums are over all measurements that have non-negligible MRF at the pixel.

For implementation in the CETB, fine map grid resolutions were selected for each channel according to Table 1. Details of how these grid factors were determined are given below.

Table 1: CETB fine resolution grid definitions

Channel Frequency	Fine Grid Scale Factor	Fine Grid Resolution
6.6*	2	12.5 km
10.7*	4	6.25 km
18*, 19, 21, 22	8	3.125 km
37	8	3.125 km
85**, 91***	8	3.125 km

*SMMR only, **SSM/I only, ***SSMIS only

1.3.1 Backus/Gilbert Method

Backus and Gilbert (1967; 1968) developed a general method for inverting integral equations, which can be applied to solving sampled signal reconstruction problems (Caccin et al., 1992). First applied to radiometer data by Stogryn (1978) the Backus/Gilbert method has been used extensively for extracting vertical temperature profiles from radiometer data (Poe, 1990). It has also been used for spatially interpolating and smoothing data to match the resolution between different channels (Robinson et al. 1992), and improving the spatial resolution of surface brightness temperature fields (Farrar and Smith, 1992; Long and Daum, 1998; Chakraborty et al., 2008). Antenna pattern deconvolution approaches have been also done (Sethmann et al., 1994; Swith et al., 1990).

In application to reconstruction, the essential idea is to write an estimate of the surface brightness temperature at a particular pixel as a weighted linear sum of measurements that are collected "close" to the pixel, i.e., using the notation developed in the previous section, the estimate at the jth pixel is

$$\hat{a}_j = \sum_{i \in nearby} w_{ij} T_i$$

Equation 9

where the w_{ij} are weights selected so that

$$1 = \sum_i w_{ij} \quad \forall j$$

Equation 10

There is no unique solution for the weights; however, regularization permits a subjective tradeoff between the noise level in the image and in the resolution (Long and Daum, 1998). Regularization and selection of the tuning parameters are described in detail by Caccin et al. (1992) and Robinson et al. (1992). There are two tuning parameters, an arbitrary dimensional parameter and a noise-tuning parameter γ. The dimensional parameter affects the optimum value of tuning parameter γ. Following Robinson et al. (1992), we set the dimensional-tuning parameter to 0.001. The noise-tuning parameter, which can vary from 0 to $\pi/2$, controls the tradeoff between the resolution and the noise. The value of γ must be subjectively selected to "optimize" the resulting image and depends on the measurement noise (standard deviation, ΔT) and the "penalty function" chosen. For use in the CETB, we use the constant penalty function J=1 the reference function F=1 over the pixel of interest, and 0 elsewhere as used by Farrar and Smith (1992) and Long and Daum (1998).

Using our notation, for a particular pixel j, define the squared signal reconstruction error term Q_R

$$Q_R = \left(\sum_{i \in nearby} w_{ij} h_{ij} - 1 \right)^2$$

Equation 11

and the noise error term

$$Q_N = \vec{w}^T \mathbf{E} \vec{w}$$

Equation 12

where **E** is the T_B noise covariance matrix. We assume the noise and signal are independent. To provide a tradeoff between noise and resolution, a value for γ is included to weight the reconstruction error and the noise error in the total error *Q*, i.e.,

$$Q = Q_R \cos\gamma + \omega Q_N \sin\gamma$$

Equation 13

where ω is the dimensional tuning parameter. Since the noise realization is independent from measurement, **E** is a diagonal matrix with diagonal entries (ΔT)/2 where ΔT is the radiometer channel noise standard deviation.

The total error *Q* in Equation 3 is minimized when the weight vector for the pixel is selected as

$$\vec{w} = \mathbf{Z}^{-1}\left(\cos\gamma v_i + \frac{1-\cos\gamma \vec{u}^T \mathbf{Z}^{-1} \vec{v}}{\vec{u}^T \mathbf{Z}^{-1} \vec{u}}\right)$$

Equation 14

where

$$\vec{u}_i = \sum h_{ij} = \vec{v}_i$$
$$\mathbf{Z} = \cos\gamma \mathbf{G} + \omega \sin\gamma \mathbf{E}$$
$$\mathbf{G} = \left[h_{ij} h_{kj}\right]$$

Equation 95

Note that formulation in our case is somewhat simplified, since the grid cells have constant area. Varying γ alters the solution for the weights between a (local) pure least-squares solution and a minimum noise solution. As noted, γ must be subjectively chosen. The dimensions and measurements included in the equations are those deemed "local" according to the criteria.

In previous applications of Backus/Gilbert to measurement interpolation, (including the heritage SSM/I Pathfinder data, Armstrong et al. 1994), the measurement layout and MRF were limited to small local areas and fixed geometries to reduce computation and enable precomputation of the coefficients (Robinson et al., 1992; Galantowicz and England, 1991; Galantowicz, 1995). Azimuthally averaged antenna gain patterns have also been used (Farrar and Smith, 1992). Previous investigators (e.g., Stephens and Jones, 2002) processed the measurements on a swath-based grid. The fixed geometry yields only relatively small number of possible matrices, which can yield computational saving by permitting pre-computation of the matrices. Unfortunately, for the Earth-based grids used in this project have more variable geometries, making this approach less viable. Previous investigators (Robinson et al., 1992) have used BGI to optimally degrade the resolution of high frequency channels to "match" that of lower frequency channels. Rather than do this, we attempt to optimize the resolution of each channel independently.

For BGI processing of CETB products, we follow Long and Daum (1998) to define "nearby" as regions where the MRF is within 9 dB of the peak response. Outside this region the MRF is treated as zero. We compute the solution separately for each output pixel using the particular measurement geometry antenna pattern at the swath location and Earth azimuth scan angle. This significantly increases the computational load, but results in the best quality images.

The value of γ is subjectively selected for each channel, but held constant for each channel (on rows of Table 1). As described in more detail later we have found that the Backus/Gilbert method occasionally produces artifacts due to poor condition numbers of the matrix that needs to be inverted. To eliminate these, a median-threshold filter is defined that examines a 3x3 pixel window area around each pixel. The filter purpose is to detect "spikes" defined to be more than (TBD) 10K above the median of the pixels within the window. T_B spikes above this threshold are replaced with the median value within the window.

The gridding and reconstruction methods can be applied to all of the CETB sensors with similar performance. In this report, however, we concentrate on describing the methods as applied to a particular sensor, the Special Sensor Microwave/Imager (SSM/I).

2 Special Sensor Microwave/Imager (SSM/I)

The SSM/I is a total-power radiometer with seven operating channels, see Table 1. These channels cover four different frequencies with horizontal and vertical polarizations channels at 19.35, 37.0, and 85.5 GHz and a vertical polarization channel at 22.235 GHz (Hollinger et al., 1990). An integrate-and-dump filter is used to make radiometric brightness temperature measurements as the antenna scans the ground track via antenna rotation (Hollinger, 1989). As specified by Hollinger et al. (1987) the 3 dB elliptical antenna footprints range from about 15-70 km in the cross-scan direction and 13-43 km in the along-scan direction depending on frequency. First launched in 1987, SSM/I instruments have flown on multiple spacecraft continuously until the present on the Defense Meteorological Satellite Program (DMSP) (F) satellite series.

Table 1: SSM/I Channel Characteristics (Hollinger, 1987)

Channel Name	Polarization	Center Frequency (GHz)	Bandwidth (MHz)	3 dB Footprint Size (km)	Channel ΔT* (K)
19H	H	19.35	125	43 × 69	0.42
19V	V	19.35	125	43 × 69	0.45
22	V	22.23	300	40 × 60	0.74
37H	H	37	750	28 × 37	0.38
37V	V	37	750	20 × 37	0.37
85H	H	85.5	2000	13 × 15	0.73
85V	V	85.5	2000	13 × 15	0.69

* Estimated instrument noise for the F08 SSM/I. Actual varies between sensors.

The SSM/I scanning concept is illustrated in Figure 1. The antenna spin rate is 31.6 rpm with an along-track spacing of approximately 12.5 km. The measurements were collected at a nominal incidence angle of approximately 53°. The scanning geometry produces a swath coverage diagram as shown in Fig. 2. A close-in view of the arrangements of the antenna footprints on the surface for different antenna azimuth angles is shown in Fig. 3. The integrate and dump filters are 3.89 ms long for the 85 GHz channels and 7.95 ms long for the other channels. The time between samples is 4.22 ms long for the 85 GHz channels and 8.44 ms long for the other channels.

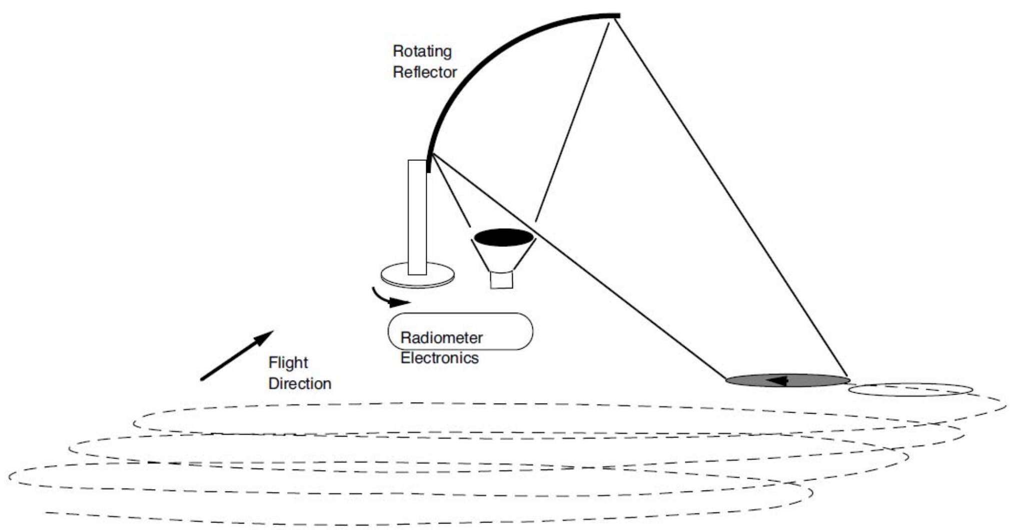

Figure 1. Illustration of the SSM/I scanning concept. The antenna and feed are spun about the vertical axis. Due to the along-track translation of the nadir point resulting from spacecraft motion in its orbit, the resulting scan pattern on the surface is an overlapping helix. Due to interference from the spacecraft structure, only part of the rotation is useful for measuring the surface T_B, see Fig, 2. The rest of the rotation time is used for calibration. The observation incidence angle is essentially constant as the antenna scans the surface. (Long, 2008)

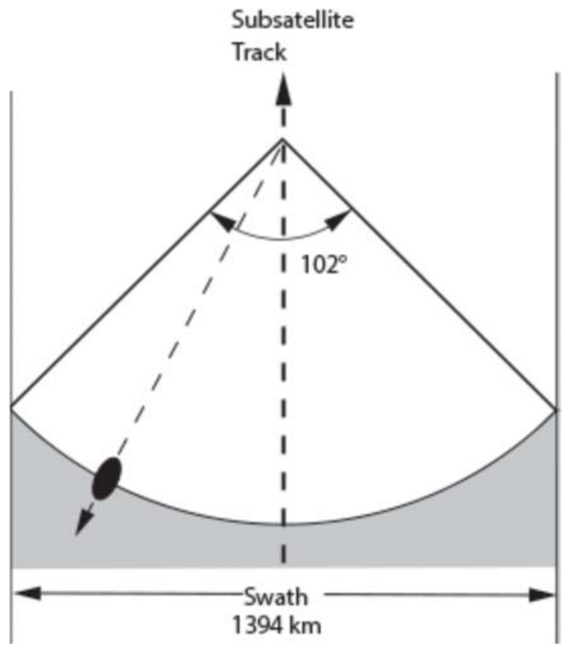

Figure 2. SSM/I coverage swath. The dark ellipse schematically illustrates the antenna 3dB response mainlobe on the surface for a particular channel at a particular antenna scan angle as illustrated by the light dashed line. The orientation of the ellipse varies relative to the ground track due to the rotation of the antenna, which is centered at the top of the diagram. The observation swath is defined the rotation of the antenna through a total scan angle range of 102°. The dark dashed line represents the spacecraft nadir ground track. The measurement incidence angle remains essentially constant during the scan. This diagram is for the aft-looking F08 SSM/I. Later SSM/Is looked forward but had the same swath width.

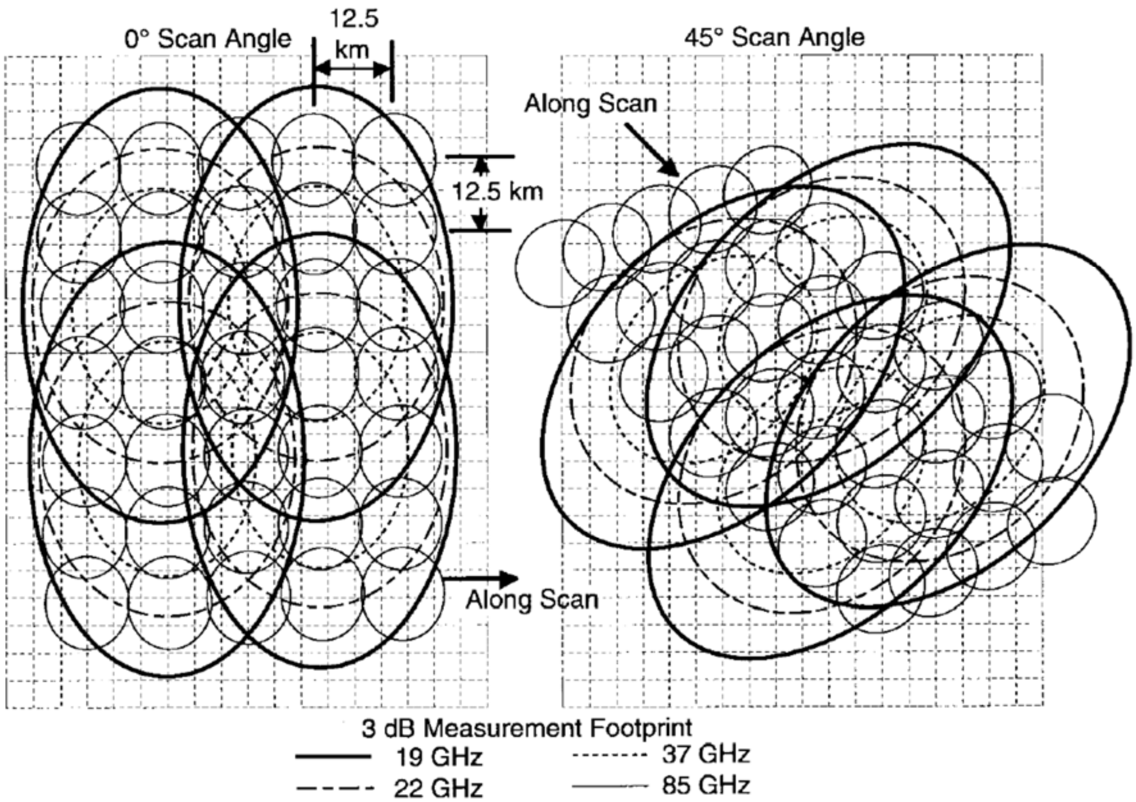

Figure 3. Illustration of the individual footprints of the various channels shown at two different scan angles. Only footprints for the V pol channels are shown. Note the change in orientation of the footprints with respect to the Earth-fixed underlying grid. (Long and Daum, 1998)

2.1 Approximating the Spatial Response Function

This section describes how the radiometer spatial measurement response function (MRF) is modeled. Let $T_{A'}$ be the antenna brightness temperature measurement corrected to the surface. The observed brightness can be modelled as an ideal noise-free $T_{A'}$ value pulse "noise" that is due to the intrinsic variability of a brightness temperature measurement.

The implicit assumption employed in image reconstruction is that a given radiometer measurement $T_{A'}$ can be modelled as

$$T_{A'} = \iint MRF(x,y)\, T_B(x,y)\, dx\, dy + noise$$

Equation 16

where the noise term is the result of the intrinsic variability of a brightness temperature measurement. The measurements $T_{A'}$ are the integral of the product of the MRF (which may be different for each measurement) and the surface brightness temperature. The "nominal" resolution of the $T_{A'}$ measurements is typically considered to be the size of the 3dB or half-power response pattern of the MRF. The goal is to estimate $T_B(x,y)$ for each channel at the highest resolution possible from the measurements $T_{A'}$ at the various sample locations collected by the sensor. Note that images are separately created for each channel.

The reconstruction algorithm requires a model (i.e., a description) of the MRF in order to generate enhanced-resolution images. Ideally, the model requires knowledge of the sensor antenna pattern for the channel. Given the antenna pattern, and information about the rotation rate, the "smeared" antenna pattern can be computed, from which the MRF is derived (CETB ATBD, 2014). However, the amount of information about the detailed antenna pattern is often limited. In some cases (e.g., SMMR), all that is known is the approximate size of the 3 dB or half-power footprint. These elliptical footprints have their semi-major axis along the boresite direction, while the semi-minor axis is in the along-rotation direction. The orientation of the footprint semi-major axis varies with the antenna rotation angle, see Figures 1-3.

To describe the antenna patterns for each sensor, we adopt an approximate model for the MRF based on a rotated, two-dimensional Gaussian function aligned with the footprint orientation where the half-power points of the Gaussian correspond to the footprint sizes reported for each sensor. The Earth azimuth angle of each measurement with respect to north, see Figure 4, is either provided in the data set or derived. This is the angle (on the ground) from true North to the vector from the sensor to the measurement center location; it describes the rotation angle of the elliptical footprint relative to north. An illustrative example of the result is shown in Figure 5. As discussed in Section 4, based on the sensitivity of the reconstruction when regularization is employed, this model is adequate for our purposes.

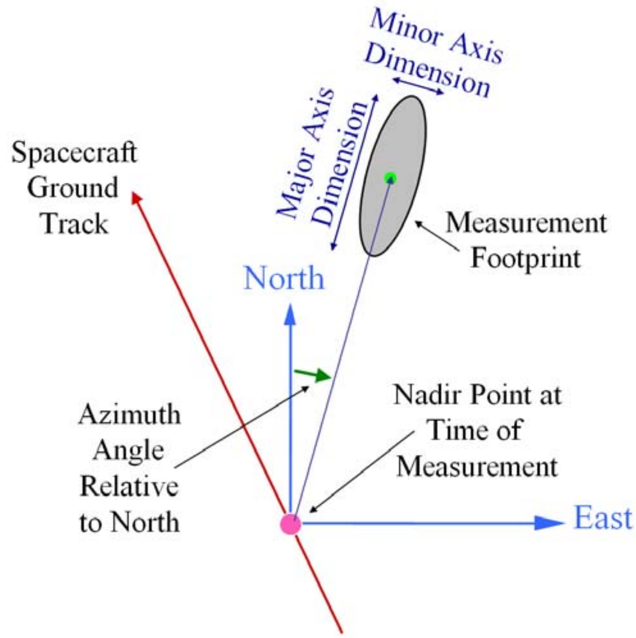

Figure 4 An illustration of the geometry of the a general Gaussian model for the MRF for a radiometer. The figure is not to scale. All vectors here are in the same plane with the "Nadir Point" being the Spacecraft Nadir Point.

The algorithm for computing the MRF is given here. A grid of pixels centered at the measurement center is defined. The grid is chosen large enough so that MRF gain at the edges of the grid is no more than a small threshold, e.g. -30 dB of the MRF peak. Then, using the map projection, the relative vector distance from the measurement center to the center of each pixel is computed as the vector $\mathbf{X}_{rel}=[x_r,y_r]^T$. This vector is rotated by the azimuth angle φ (relative to north) of the ellipse. The rotated system is

$$\mathbf{X}=[x,y]^T=R(\varphi)\,\mathbf{X}_{rel}$$

where

$$R(\varphi)=\begin{bmatrix}\cos(\varphi) & -\sin(\varphi)\\ \sin(\varphi) & \cos(\varphi)\end{bmatrix}$$

Define the length of the semi-major axis in km as L_j and the semi-minor axis as L_n. The MRF gain G at the center of the pixel is then

$$G=\ln(1/2)\exp[\,(2x/L_j)^2+(2y/L_n)^2\,]$$

Equation 107

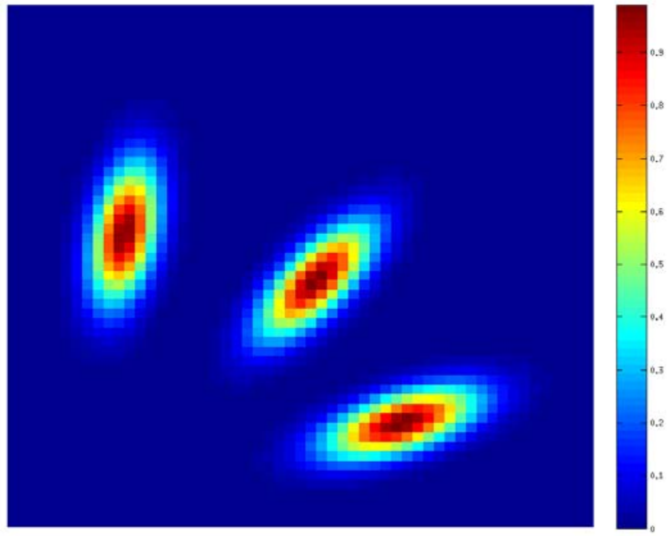

Figure 5. An illustration of a general Gaussian model for the MRF for a particular radiometer. Shown is the MRF in linear space for several antenna rotation angles. The figure is not to scale. The color scale is unit-less gain which varies from 0 to 1.

An illustrative example of the result for several values of φ is shown in Figure 5. Note that half-power point of G corresponds to the specified ellipse semi-major and semi-minor axes.

While this simplified model for the MRF may not exactly model the true MRF, as discussed in Section 4, based on the sensitivity of the reconstruction when regularization is employed, this model is adequate for our purposes.

2.2 SSM/I Reconstruction Simulation

Reconstruction algorithms that generate 2D gridded images from raw measurements are characterized by a tradeoff between noise and spatial resolution. Our goal is to estimate an image of the surface $T_B(x,y)$ from the sensor T_B measurements. The "nominal" resolution of the T_B measurements is typically considered to be the size of the 3dB response pattern of the MRF. With "drop-in-the-bucket" imaging, the effective resolution can be no finer than the effective resolution of the measurements. However, reconstruction techniques can yield higher effective resolution if spatial sampling requirements are met.

Based on the description of the SSM/I measurement geometry given previously, the ideal locations of antenna boresite at the center of the integration period can be computed. Simulated locations are plotted for a particular channel in Figure 9. These define the "measurement locations".

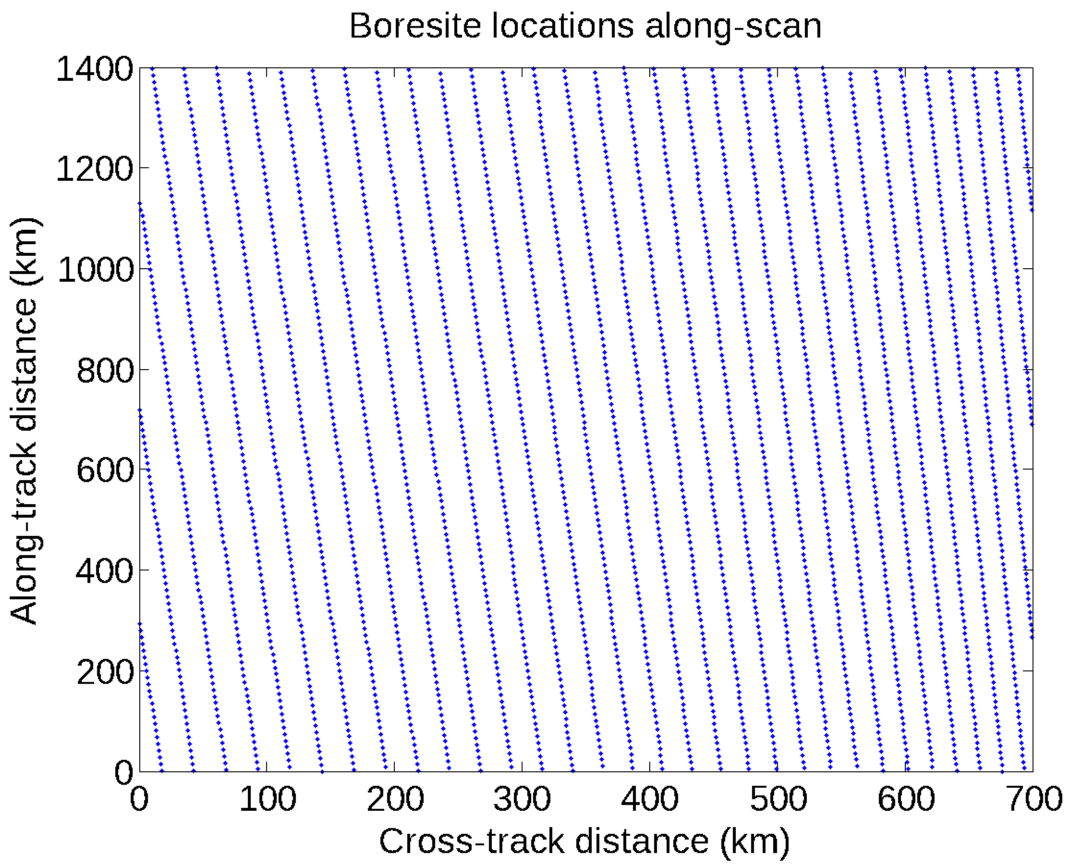

Figure 9 Illustrations of the measurement locations (boresight location of the antenna pattern at the center of each measurements integration period) for the simulated SSM/I measurements. Only part of the coverage swath is shown. Note that the axes have different scales and that the nominal spacing is approximately 25 km in both directions.

Images calculated in the polar regions combine measurements from multiple passes of the spacecraft over the same area. While the sampling for a single pass is on a regular grid, the sampling from multiple overlapping passes tends to be less regular. For example Figure 10 illustrates the sampling resulting from two overlapping passes. A zoomed view of the sampling compared to a 25 km grid is shown in Figure 11. The variation in sample locations with each 25 km grid element is apparent in the zoomed image.

Given these sample locations, and their corresponding spatial response functions, the goal is to use signal reconstruction techniques to estimate the surface brightness temperature from the measurements.

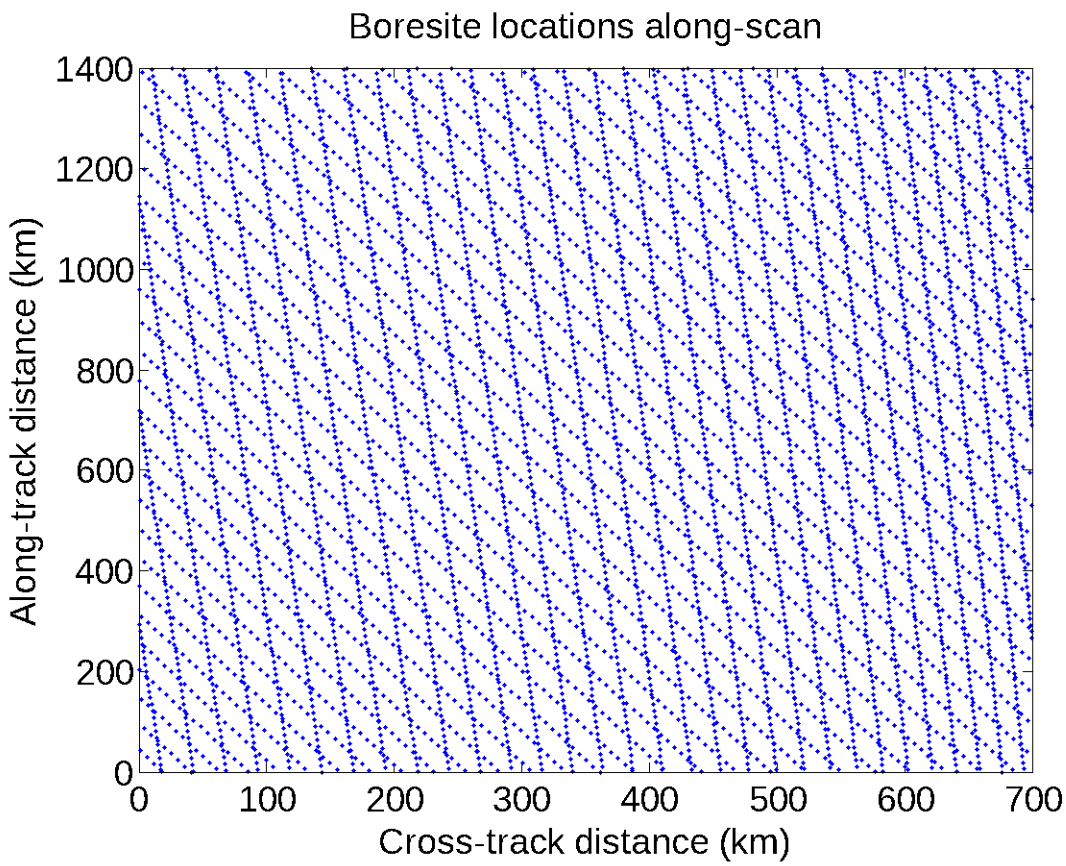

Figure 10 Illustrations of the measurement locations (boresight location of the antenna pattern at the center of each measurements integration period) for two overlapping passes. Only part of the coverage swath is shown. See caption for Figure 9.

Fortunately, there is a well-defined theory of signal reconstruction based on irregular sampling which can be applied to our problem. The three primary techniques applicable to our problem are Backus-Gilbert (BG) inversion (Backus and Gilbert, 1967; 1968), the iterative Scatterometer Image Reconstruction (SIR) technique (Early and Long, 2001; Long and Daum, 1998), and the weighted measurement approached termed AVE (Long et al., 1993). As shown in these papers, there is a tradeoff between signal reconstruction accuracy and noise enhancement. Regularization can reduce noise enhancement and signal artifacts, at the expense of resolution. A comparison of Backus-Gilbert and the iterative Scatterometer Image Reconstruction (SIR) technique for radiometer image reconstruction is given in Long and Daum (1998), where SIR is found to provide similar performance with significantly less computation required.

Regularization in SIR is implemented by terminating the iterative reconstruction early, i.e., prior to final convergence. As shown below, this allows us to minimize noise enhancement while improving the signal reconstruction. Note that AVE is the first iteration of SIR.

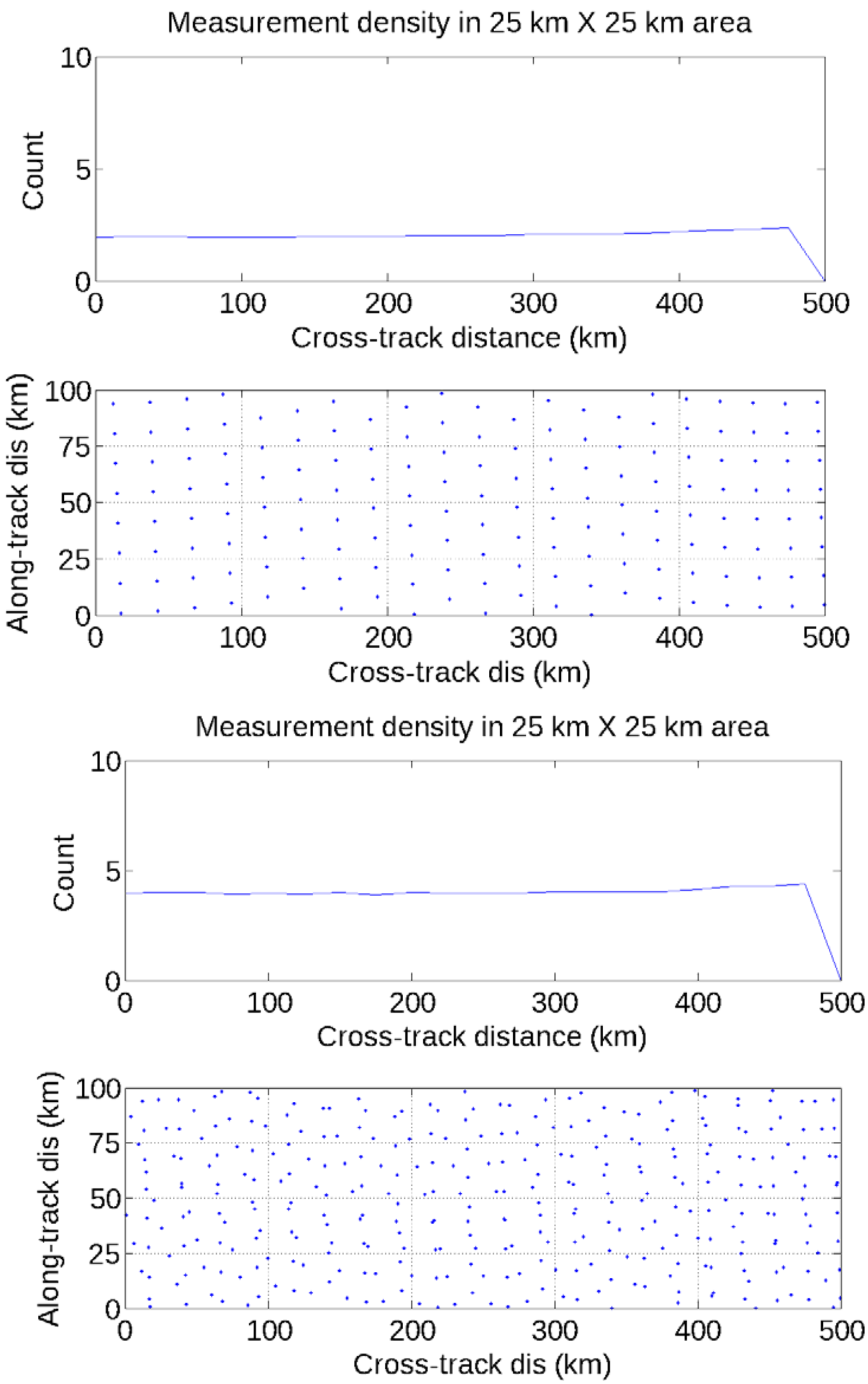

Figure 11 Illustrations of the measurement locations within the coverage swath for the SSM/I 37 GHz channel for (top) one pass and (bottom) two passes.   Plots of the average density of measurements as function of cross track distance are also shown. For clarity, only one side of the nadir line is shown. Nominal measurement spacing for a single pass is approximately 25 km.

To demonstrate and compare the performance of the various reconstruction techniques, it is helpful to use simulation. The results of these simulations inform the tradeoffs needed to select processing algorithm parameters. A simple (but realistic) simulation of the SSM/I geometry and spatial response function is used to generate simulated measurements of a synthetic image. From both noisy and noise-free measurements, non-enhanced (GRD or Grd), AVE (or Ave), and SIR images are created, with error (mean, and root-mean-square [RMS]) determined for each case. This is repeated separately for each channel. Since the footprint sizes of the 19 and 22 GHz channels are similar (see Appendix Table 2.2-1), and the footprint sizes for the different polarizations at a given frequency are essentially the same, only the 19, 37, and 85 GHz H-pol channels are considered. While there is some sensitivity in the results to the assumed noise level, it is not large and so for convenience the noise is assumed to have a standard deviation of 1 K for all channels.

Two different pass cases are considered: the single pass case and the case with two overlapping passes. The general conclusions are the same for both cases, so the two pass case is emphasized. Finally, we need to determine the scale factor for the pixels for each channel. Note that the product pixel size is restricted to fractional powers of two of 25 km, i.e. the pixel size P_s in km is given by

$$P_s = \frac{25}{2^{(N_s)}}$$

where N_s is the pixel size scale factor which is limited to values of 2, 3, or 4. The set of potential values of P_s are 6.25, 3.125, and 1.5625 km. For the simulation, pixels are square.

An arbitrary band-limited "truth" image is generated with some "spots" of varying sizes, some smooth areas of constant T_B and some gradient area to help visualize the error, see Fig. 12. The choice of a truth image has some effect on the results, but for expedience we use only a single true image.

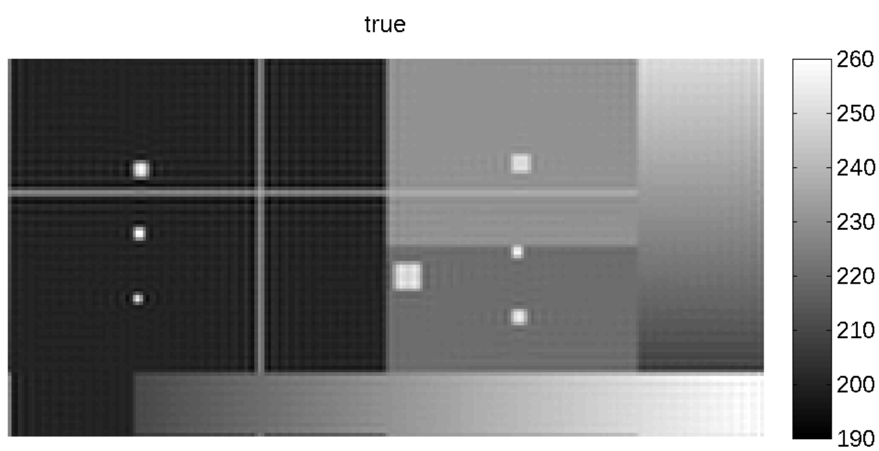

Figure 12. Example synthetic "truth" image for Ps=3.125 km. Units are K. Image has been bandpass filtered to 10 km effective resolution, which accounts for the Gibbs phenomena at boundaries. Features where were arbitrarily selected to illustrate different target sizes.

As described earlier, the MRF is modeled with a Gaussian whose 3dB (half-power) point matches the footprint size given in Table 1. The orientation of the ellipse varies over the swath according to the look direction as suggest in Figs. 4 and 5. To apply the MRF in the processing the MRF is centered at center of the nearest neighbor pixel to the measurement location. The values of the discrete MRF are computed at the center of each pixel in a box surrounding the pixel center. The size of the box is defined to be the smallest enclosing box for which the sampled antenna pattern is larger than a minimum gain threshold of -30 dB relative to the peak gain. A second threshold (typically -9 dB) defines the gain cutoff used with in the SIR and BGI processing. The latter threshold defines the so-called Nsize parameter used by Long and Daum (1998).

The image pixel size defines how well the MRF can be represented in the reconstruction processing and the simulation. Since in this simulation we want to evaluate different pixel sizes, a representative plot of the MRF sampling for each channel for each pixel size under consideration is shown in Fig. 13. Note that footprint sizes for each channel are the same, but the pixel sizes vary.

GRD images are created by collecting and averaging all measurements whose center falls within each 25 km grid element. The resulting GRD image is then pixel-replicated to match the number of pixels of the AVE and SIR images. We define the pixel-replicated image as the NON (sometimes written as Non) image. Separate images are created for both noisy and noise-free measurements. Error statistics (mean, standard deviation, and RMS) are computed from the difference between the “truth” and estimated images. The noise-only RMS statistic is created by taking the square root of the difference between the squared noisy RMS and the squared noise-free RMS.

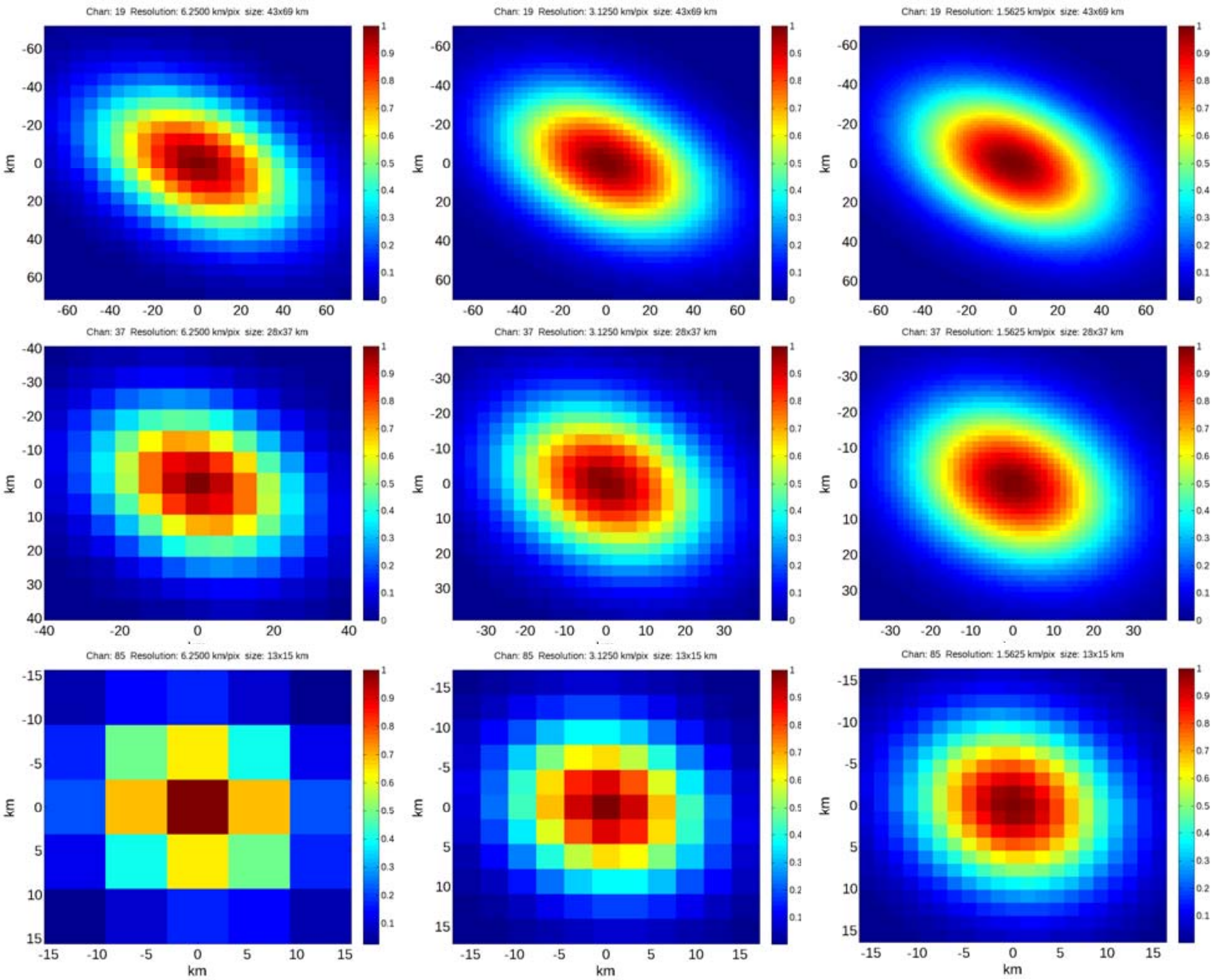

Figure 13. Illustrative sampled MRF for channels (top row) 19 GHz, (middle row) 37 GHz, (bottom row) 85 GHz and pixels sizes (left column) 6.25 km, (middle column) 3.125 km, (right column) 1.5625 km. The MRF size in km is the same for a given channel (row). The pixel sizes are the same in each column, though the area covered by the image varies. The axes are in km and vary by image. The color scale is unit-less gain. In the plots shown here, the MRF is normalized to one at the peak.

Figure 14 illustrates a typical SIR simulation result. It shows the true image, and both noise-free and noisy NON, AVE, and SIR images. The error statistics for this case are given in Table 3. For this pixel size, the image size is 448 x 224. In all cases the error is effectively zero mean. The non-enhanced results have the larger errors, with the Ave results slightly less. The RMS error is the smallest for the SIR results. Visually, NON and AVE are similar, though SIR images better define edges. The spots are much more visible in the SIR images than in the NON images, though the SIR image has a higher apparent noise "texture".

Table 3. Two pass simulation results statistics for 37 GHz, Ps=3.125 (in K), with 20 SIR iterations.

Case	Mean	STD	RMS
N-F Non	0.00	4.34	4.34
N-F Ave	0.00	4.33	4.33
N-F SIR	0.00	3.62	3.62
Noisy Non	0.01	4.38	4.38
Noisy Ave	0.01	4.34	4.34
Noisy SIR	0.01	3.69	3.69

Theoretically, SIR should be iterated to convergence to ensure full signal reconstruction. This can require hundreds of iterations (Early and Long, 2001). However, continued SIR iteration also tends to amplify the noise in the measurements. By truncating the iteration we can trade off signal reconstruction accuracy and noise enhancement. Truncated iteration results in the signal being incompletely reconstructed, though the reconstruction error declines with further iteration.

To understand the tradeoff between number of iterations and signal and noise, Figure 15 shows noisy and noise-free SIR images for several different iteration numbers. (Recall that AVE is the first iteration of SIR.) Note that the number of iterations is increased, the edges are sharpened and the spots become more evident. Figure 16 plots the mean, standard deviation, and RMS errors versus iteration. Also shown in this figure are the errors for the NON and AVE (first iteration of SIR) images. The noise texturing also increases. We thus conclude that while iteration improves the signal, the iteration cannot be too long to avoid over-enhancing the noise.

Plotting the signal reconstruction error versus noise power enhancement as a function of iteration number in Fig. 17 can help make a choice for the number of iterations that balances signal and noise performance. Note that the NON result is much noisier than AVE, and that the signal error improves with each iteration of SIR. Noting that we can stop the SIR iteration at any point, we somewhat arbitrarily choose a value that provides good signal performance and only slightly degraded noise performance, 20 iterations in this case. This is the value used in Table 3, where we see that the overall error performance is still better than the NON result.

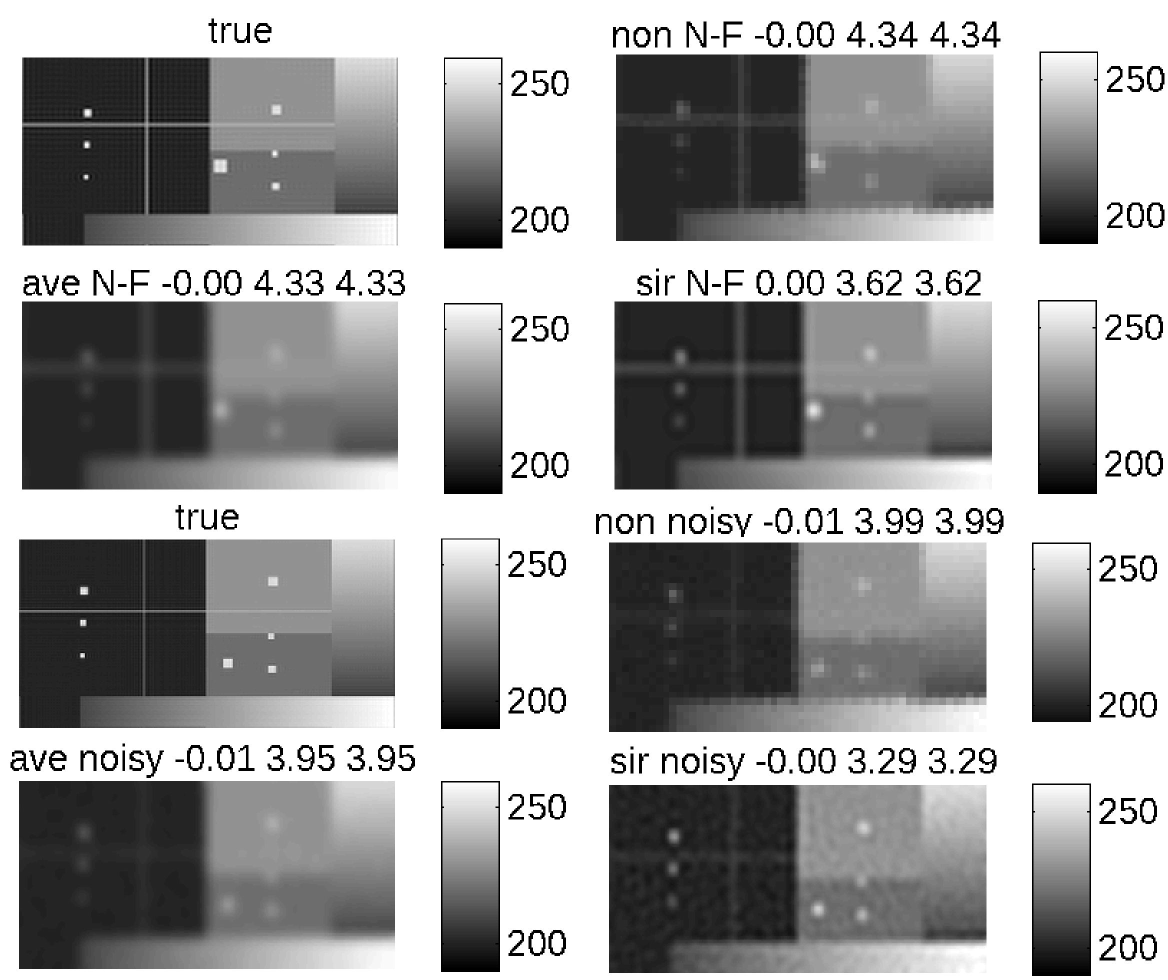

Figure 14. 37 GHz, dual-pass, Ns=3 simulation results for (upper two rows) noise-free measurements and (lower two rows) noisy measurements. SIR uses 20 iterations. The numbers on the top show the mean, std, and RMS error values compared to the true.

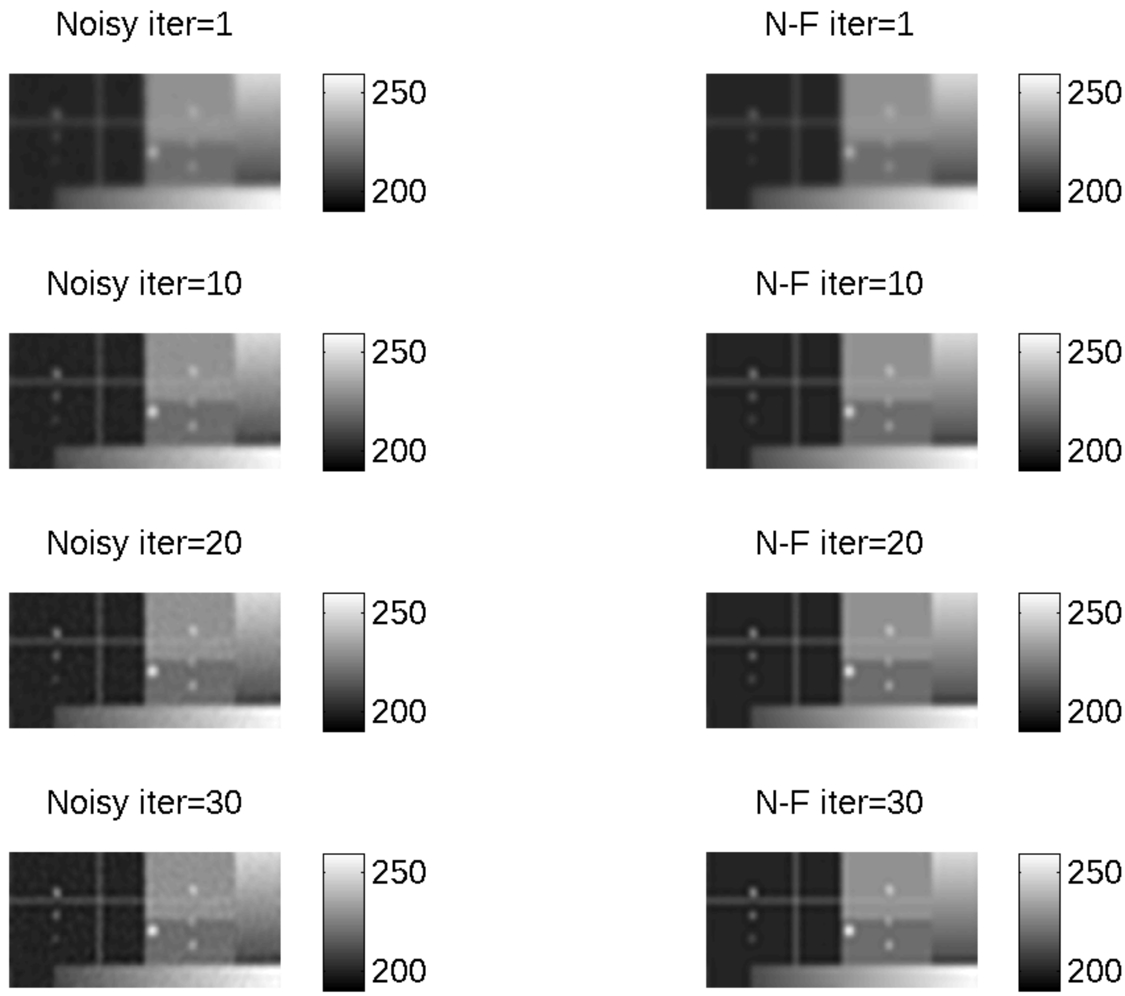

Figure 15. 37 GHz, dual-pass, Ns=3 SIR images for different iterations for (left column) noisy measurements and (right column) noise-free measurements.

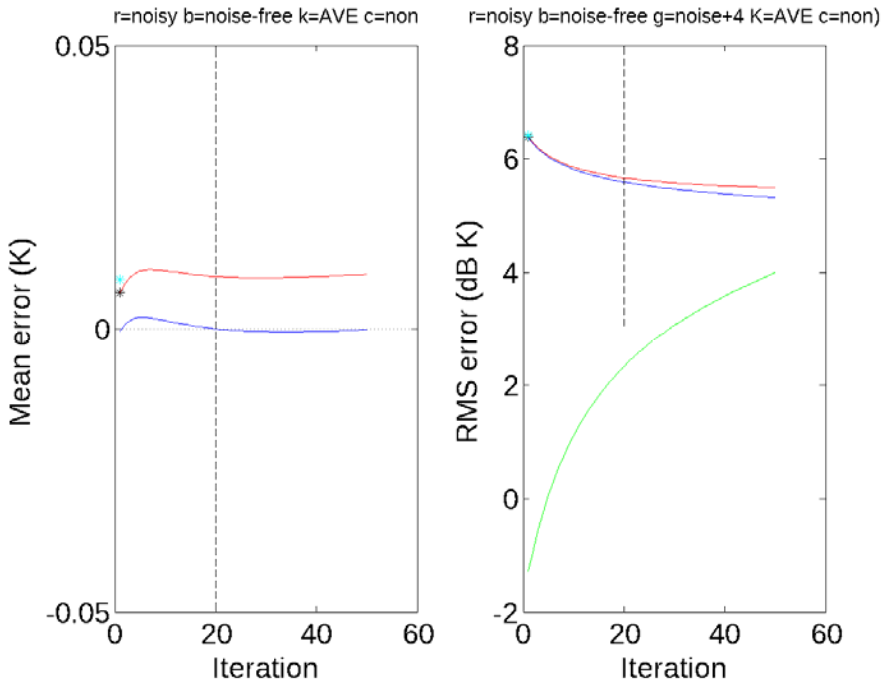

Figure 16. 37 GHz, dual-pass, Ns=3 SIR image error versus iteration number. (left) mean error. (right) RMS error. The red line is the noisy measurement case, while the blue line is the noise-free measurement case. Green is the noise power, computed from the difference between the noisy and noise-free cases. The cyan star is the error for the NON image, while the black star is for AVE (which may be under the cyan star). The "optimum" (minimum error) number of iterations occurs at the minimum of the red curve. For reference, the dashed vertical line is shown at 20 iterations.

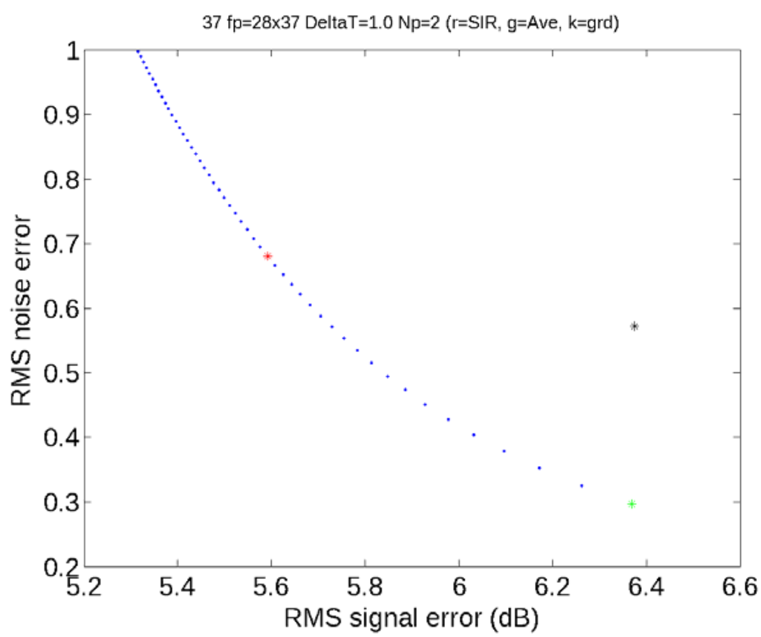

Figure 17. 37 GHz, dual-pass, Ns=3 Change in SIR image error with increasing versus iteration number. RMS noise power versus RMS signal error for each iteration, which extends from right to left. The black star in the NON result, while the green star is the AVE result. The red star is SIR at 20 iterations.

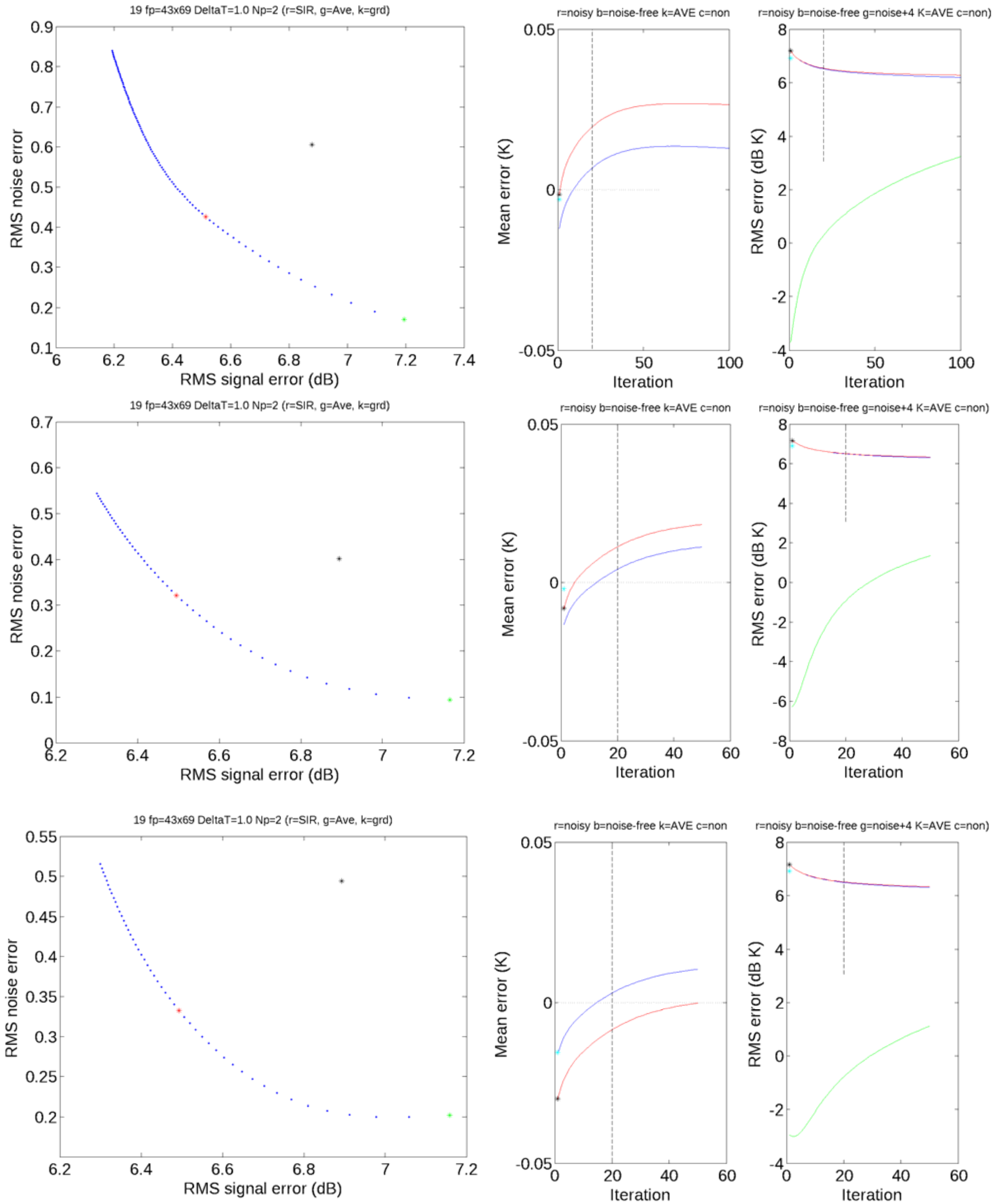

Figure 18. 19 GHz, dual-pass, image error versus iteration number for (top) Ns=2, (middle) N=3, (bottom) Ns=4. RMS noise power versus RMS signal error for each iteration, which extends from right to left. The black star in the NON result, while the green star is the AVE result. The red star is SIR at 20 iterations.

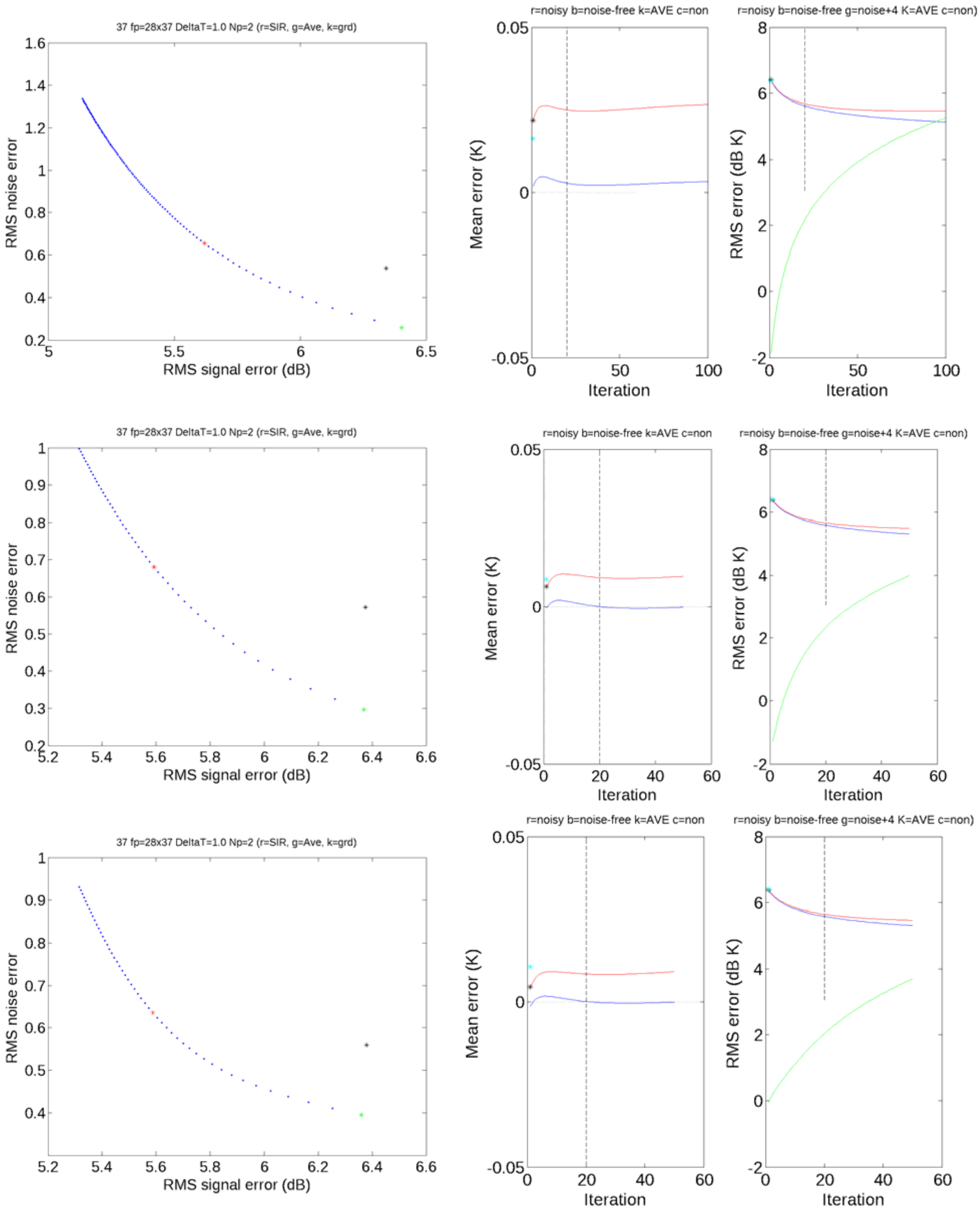

Figure 19. 37 GHz, dual-pass, image error versus iteration number for (top) Ns=2, (middle) N=3, (bottom) Ns=4. RMS noise power versus RMS signal error for each iteration, which extends from right to left. The black star in the NON result, while the green star is the AVE result. The red star is SIR at 20 iterations.

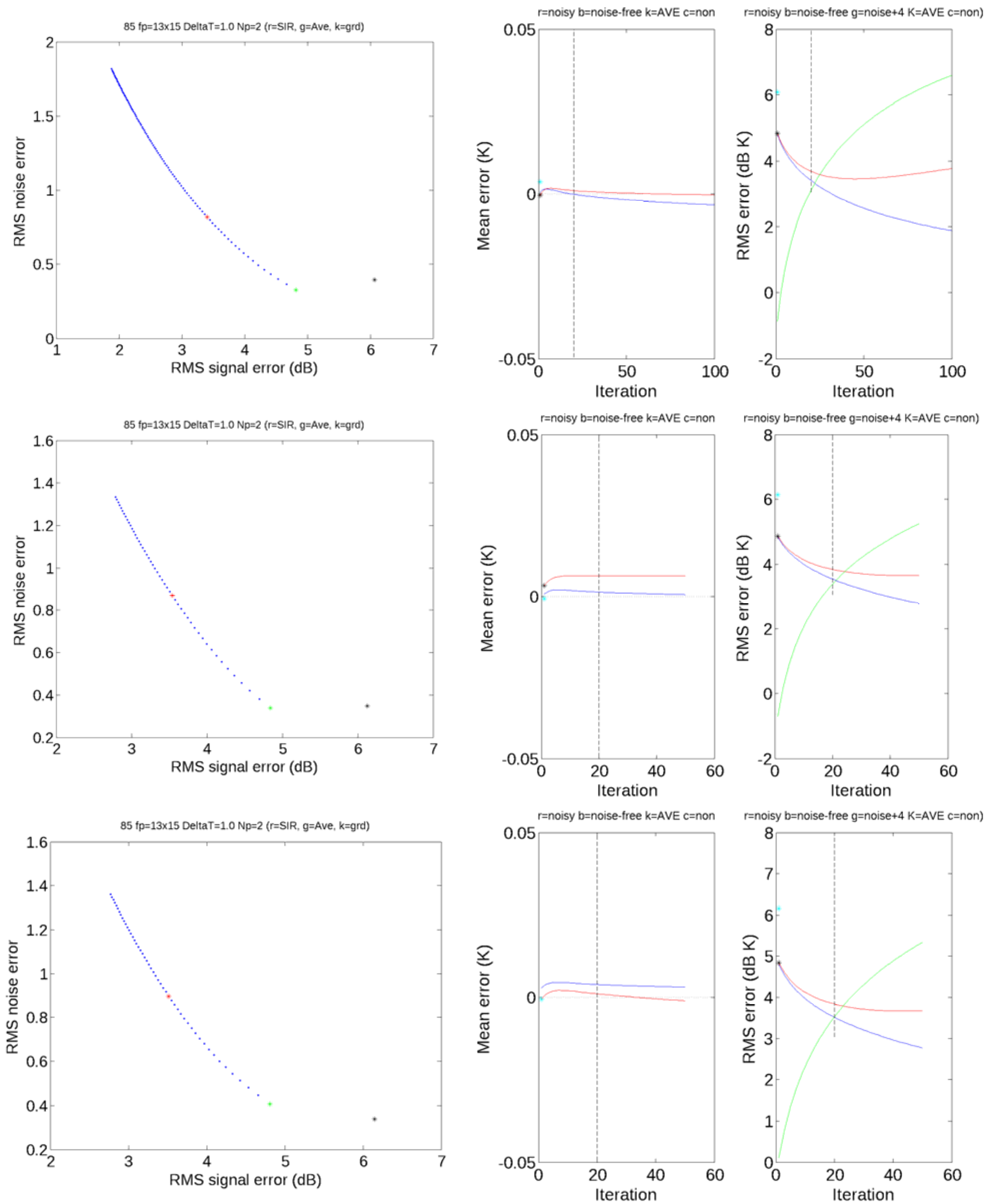

Figure 20. 85 GHz, dual-pass, image error versus iteration number for (top) Ns=2, (middle) N=3, (bottom) Ns=4. RMS noise power versus RMS signal error for each iteration, which extends from right to left. The black star in the NON result, while the green star is the AVE result. The red star is SIR at 20 iterations.

We can repeat this analysis for different values of N_s, the number of passes, and the channel number. While the numerical values of the RMS error changes, the overall ranking and relative spacing of the NON, AVE and SIR values are unchanged. Figures 18-20 shows the noise versus signal error for different values of N_s for the different channels.

Based on Figs. 18-20 the following observations can be made:

1. AVE always has somewhat better noise performance than NON.
2. AVE has slightly better signal performance than NON 37 and 85 GHz, but is worse for 19 GHz.
3. As expected, SIR always has worse noise performance than AVE, but has better signal performance
4. Depending on the number of iterations selected, SIR can always have better signal performance than both AVE and NON.
5. SIR has better signal performance than NON.
6. Iterating SIR too long causes it to have worse noise performance than NON, though the signal performance improves for longer iterations.

Since SIR is always better than AVE, but requires only a little more effort to compute, we prefer SIR to AVE. Thus the baseline for processing the highest resolution is SIR.

In general, we want to use a small N_s, to minimize computation, as well as minimize the number of iterations. Based on Nyquist criteria for sampling the response pattern, N_s=2 is the minimum useable value. With idea that we want to keep the same values for all channels, if possible, for consistency it appears that N_s=3 (i.e. P_s=3.125) will work for all channels, and that 5-20 iterations provide a reasonable tradeoff between signal and noise. Using N_s=3, Table 4 provides a performance comparison for the RMS errors of NON, AVE, and SIR for the different channels using 20 iterations. Figure 21 compares the resulting noisy simulation results. Note that although the pixel size is 3.125, the *effective* spatial resolution of the images is, of course, coarser than this. Recall that at least some of the extra pixel resolution is required to properly process the signal to meet the Nyquist signal representation requirements and represent the higher frequency content of the high resolution images. Table 5 gives the approximate number of SIR iterations for each case that results in the minimum total simulation error. It should be noted the precise minimum value depends on the exact noise realization, so this value should be considered to be a general guideline only.

Table 4. Total RMS error for noisy two pass simulation using N_s=3 (P_s=3.125) and 20 SIR iterations.

Case	NON (K)	AVE (K)	SIR (K)
19 GHz	4.91	5.21	4.47
37 GHz	4.38	4.34	3.69
85 GHz	4.12	3.07	2.42

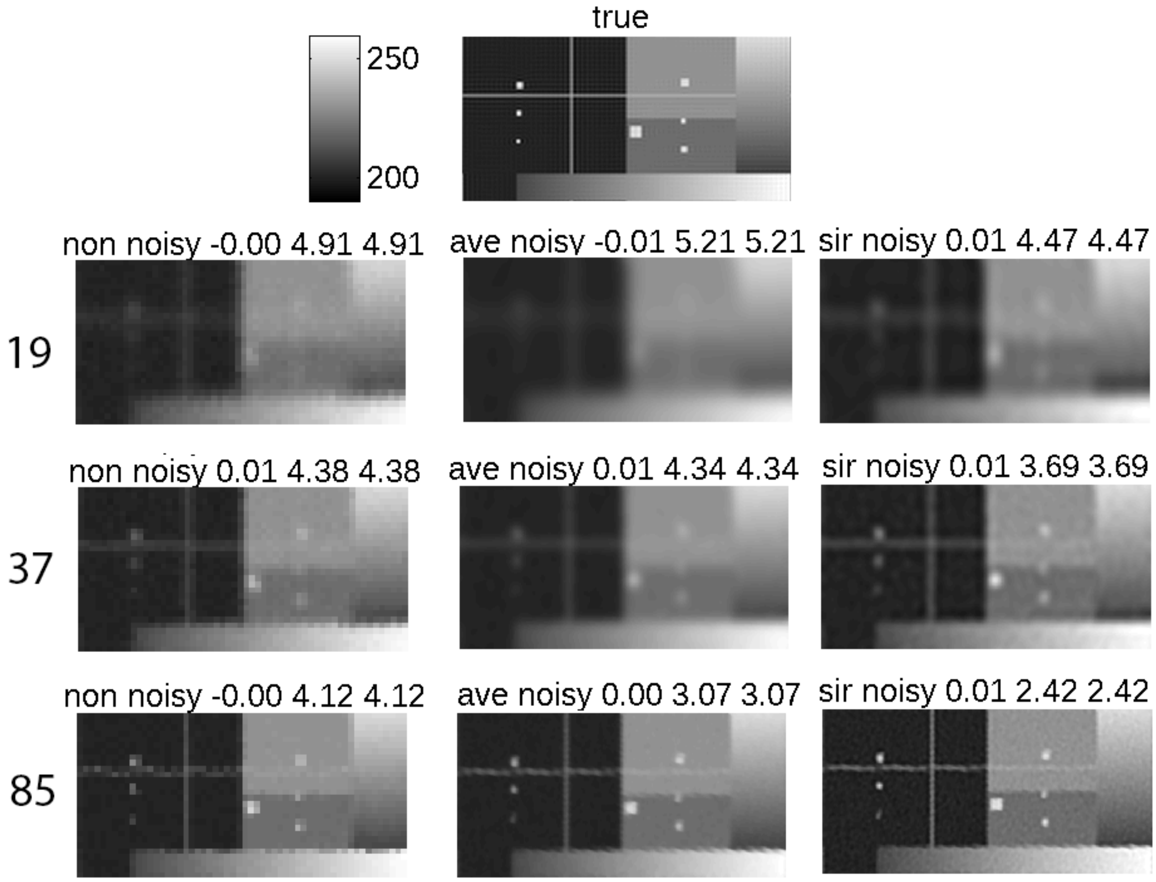

Figure 21. Comparison of (left column) NON, (center column) AVE, and (right column) SIR images for the (top full row) 19, (center full row) 37 and (bottom row) 85 GHz channels for N_s =3, 20 SIR iterations, and two passes. The top row image shows the true synthetic image.

Table 5: Recommended SSM/I SIR processing parameters by channel.

Channel	Pixel scale factor N_s and grid size P_s	SIR number of Iterations
19	(2) 6.2500 km	50*
19	(3) 3.1250 km	30*
19	(4) 1.5625 km	30*
37	(2) 6.2500 km	50*
37	(3) 3.1250 km	20*
37	(4) 1.5625 km	20
85	(2) 6.2500 km	18
85	(3) 3.1250 km	18
85	(4) 1.5625 km	15

* minimum not visible plot, so a subjective choice is made

2.3 SIR Number of Iterations and Pixel Sizes Conclusions

We find that SIR provides better spatial resolution than conventionally gridded (NON) products. SIR does enhance the noise, but this can be controlled by the number of iterations to tradeoff noise and resolution. Based on the simulation results the recommended pixel size and number of SIR iterations for each channel are given in Table 6. For reference, the SIR results for each image pixel size considered are shown in Fig. 22.

Table 6: Recommend SSM/I SIR processing parameters by channel. N_s=3.

Channel	GRD pixel size	SIR pixel size P_s	SIR number of iterations
19H	25 km	3.125 km	25
19V	25 km	3.125 km	25
22	25 km	3.125 km	20
37H	25 km	3.125 km	15
37V	25 km	3.125 km	15
85H	25 km	3.125 km	15
85V	25 km	3.125 km	15

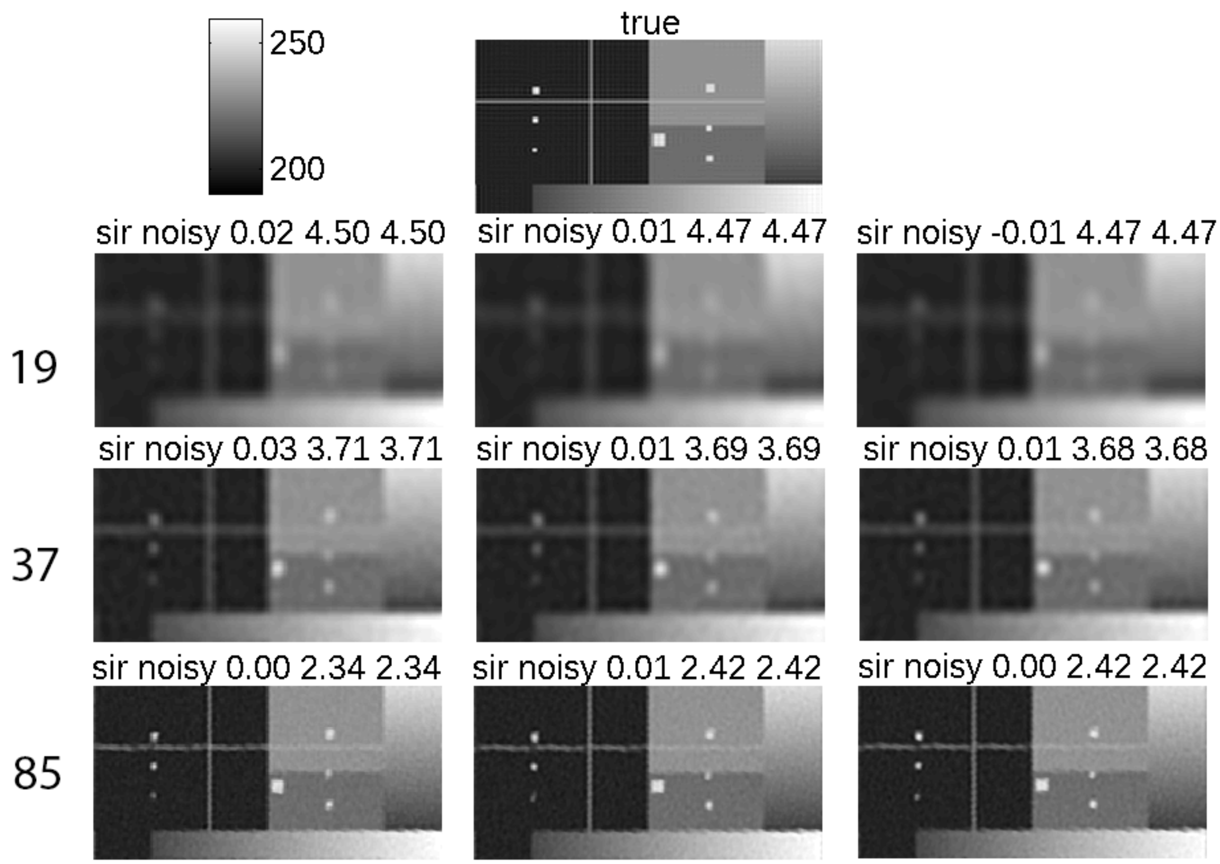

Figure 22. Comparison of SIR image results (20 iterations) for different pixel sizes and channels. Pixel sizes: (left column) 6.25 km, (center column) 3.125 km, and (right column) 1.526 km (top row). Channels: (second row) 19, (third row) 37, and (bottom row) 85. The top row image shows the true synthetic images for each pixel size. The true images vary with image pixel size due to the way they are constructed.

3 Backus-Gilbert Processing

In this section we consider the Backus-Gilbert Inversion (BGI) processing approach. The BGI approach requires significantly more computation than does SIR. Previous investigators worked on swath-based grids and were able to coarsely quantize the possible measurement positions to restrict the number of matrix inversions required. This enabled them to generate pre-computed approximate solutions (Robinson et al., 1992).

However this situation is different when working with Earth-based grids. Note from Fig. 11 that the measurement centers are irregularly arranged with respect to the Earth-located pixel grid. This limits our ability to using "preprocessing" techniques to speed the BGI computation. Further, to avoid the approximations used with fixed geometries, we prefer to use the approach developed by Long and Daum (1998) that uses the actual measurement positions and a general pixel grid so that reconstruction can be done on the Earth-located pixel grid. Note that applying BGI requires creating and inverting a matrix for each image pixel. While computationally more intense, it can yield higher effective resolution and more accurate results than the limited-area, swath grid-based techniques previously used.

Long and Daum (1998) noted that SIR and BGI produce similar results, but SIR processing is much faster than BGI. Our simulations for SSM/I confirm this conclusion. In the BGI simulations below we use the same simulated measurements as those used in the SIR experiments previously described.

As noted, BGI includes one parameter (γ) that must be subjectively selected. It controls the regularization and relative weighting between signal reconstruction and noise enhancement, see Eq. (13). The value of γ can range from 0 to $\pi/2$. Note that for simplicity in the captions and plots below, the symbols γ' or g are sometimes used that are related to γ by $\gamma = (\pi/2)\,\gamma'$ and $\gamma = \pi g$.

Figure 23 shows BGI images for various values of γ' for the 37 GHz channel with $N_s=3$. Note that for small values of γ', the noise is the most enhanced but the features are the most sharp. For larger values of γ' the noise texturing is reduced, but features are smoothed. A plot of the RMS error versus γ' is shown in Figure 24. Note that noise-free and noisy results are shown both for BGI and BGI after median filtering. Due to poorly conditioned matrices in the BGI inversion, some estimated pixels have extreme values. These can be suppressed by applying a 3x3 median filter after the BGI processing. This significantly reduces the RMS noise and artifacts in the image without significantly degrading the image quality. The median filter is edge preserving and so has minimal effect on the image quality, though some smoothing occurs.

Table 7. Two pass simulation results statistics for 37 GHz and N_s=3 (P_s=3.125 km). BGI γ'=0.45.

Case	Mean (K)	STD (K)	RMS (K)
Noisy Non	0.01	4.38	4.38
Noisy Ave	0.01	4.34	4.34
Noisy SIR	0.01	3.69	3.69
Noisy BGI	0.01	3.71	3.71
Noisy BGI – median filtered	0.01	3.70	3.70

Similar to the analysis of number of iterations for SIR, it is useful to compute the noise and signal RMS error, which varies with the value of γ'. An example for the 37 GHz channel with $N_s=3$ is shown in Figure 25. Finally a comparison of the BGI result (γ') and NON and SIR (20 iterations) is shown Fig. 26. A numerical comparison of the results is shown in Table 7. Note that even with median filtering, in this case BGI is always noisier than SIR, though the numerical differences are small.

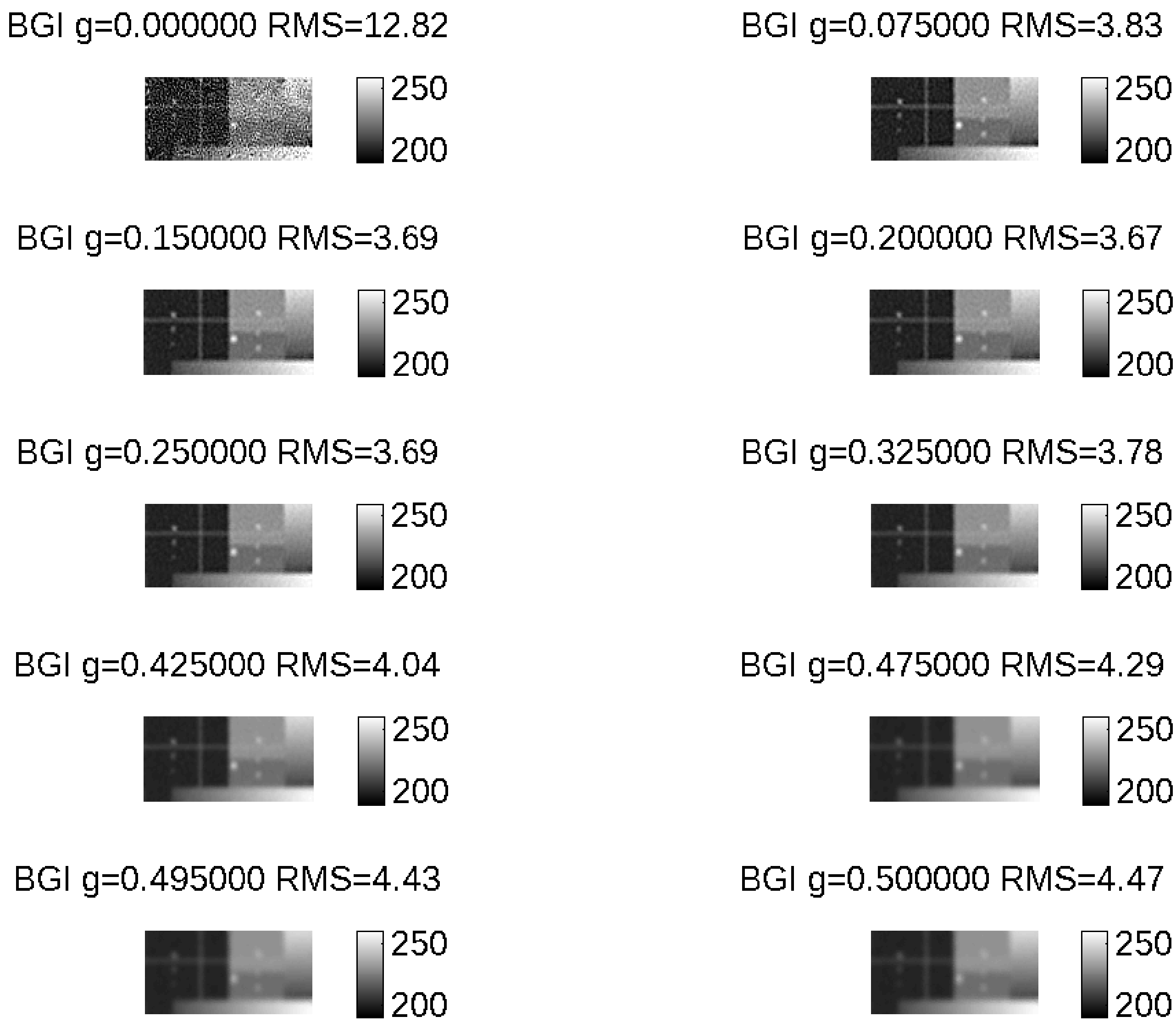

Figure 23. BGI images (no median filtering) for different values of *g* ($\gamma=\pi g$) for the 37 GHz channel with $N_S=3$. These can be compared with SIR for different iterations in Fig. 15.

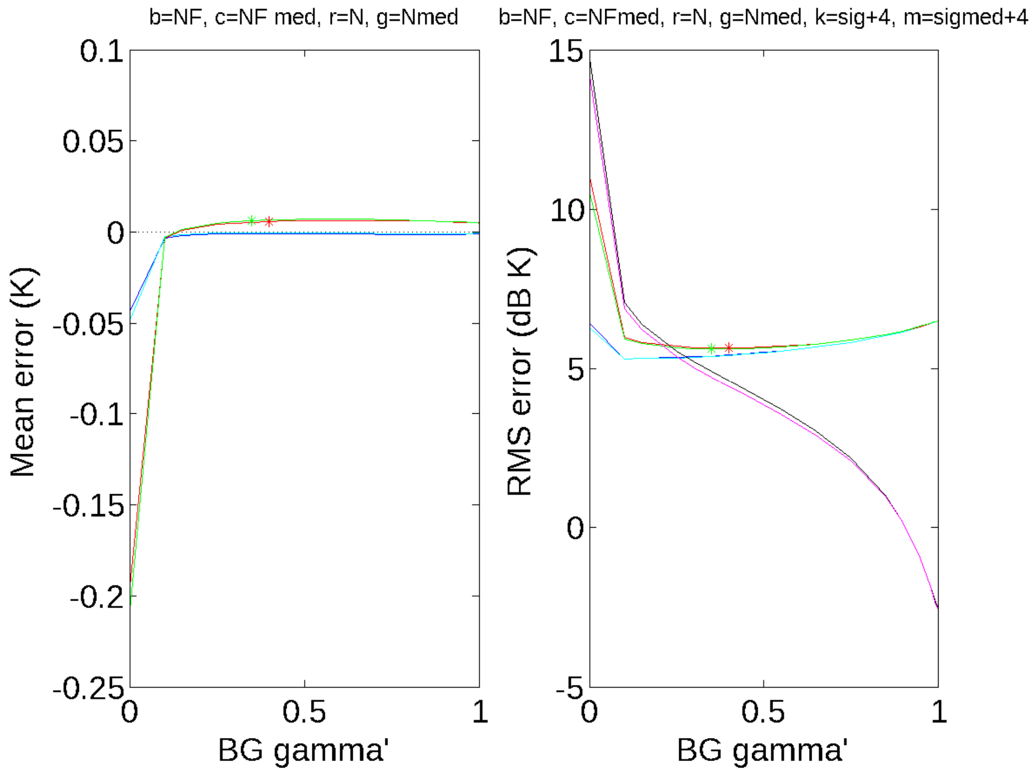

Figure 24. RMS error versus γ' for the 37 GHz channel with $Ns=3$.

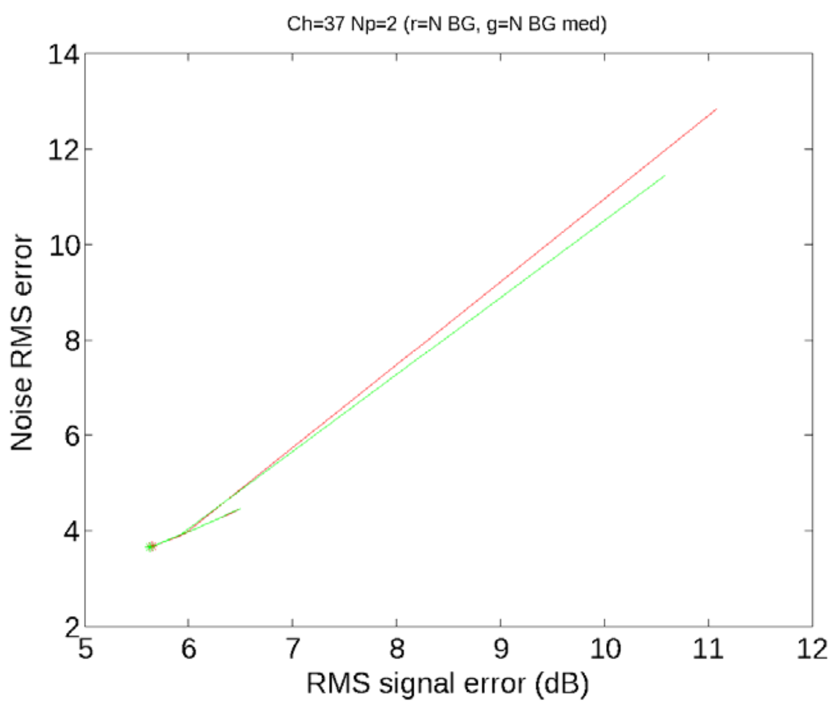

Figure 25. RMS noise versus signal for different γ' for the 37 GHz channel with $N_s=3$. The red line is noisy BGI, while the green line is noisy BGI after median filtering. γ' increases from left to right for . The optimum (i.e., the minimum RMS error) values are indicated with asterisks.

Other examples of BGI images versus different gamma parameters are shown in Figs. 27-29. Not all N_s cases are included for every channel due to excessive (and impractical) run times. All cases have a minimum total RMS error near either g=0.85 or g=0.5, so for consistency we adopt a single value γ=0.85π, for all channels and all values of N_s. This results in similar RMS performance in all cases.

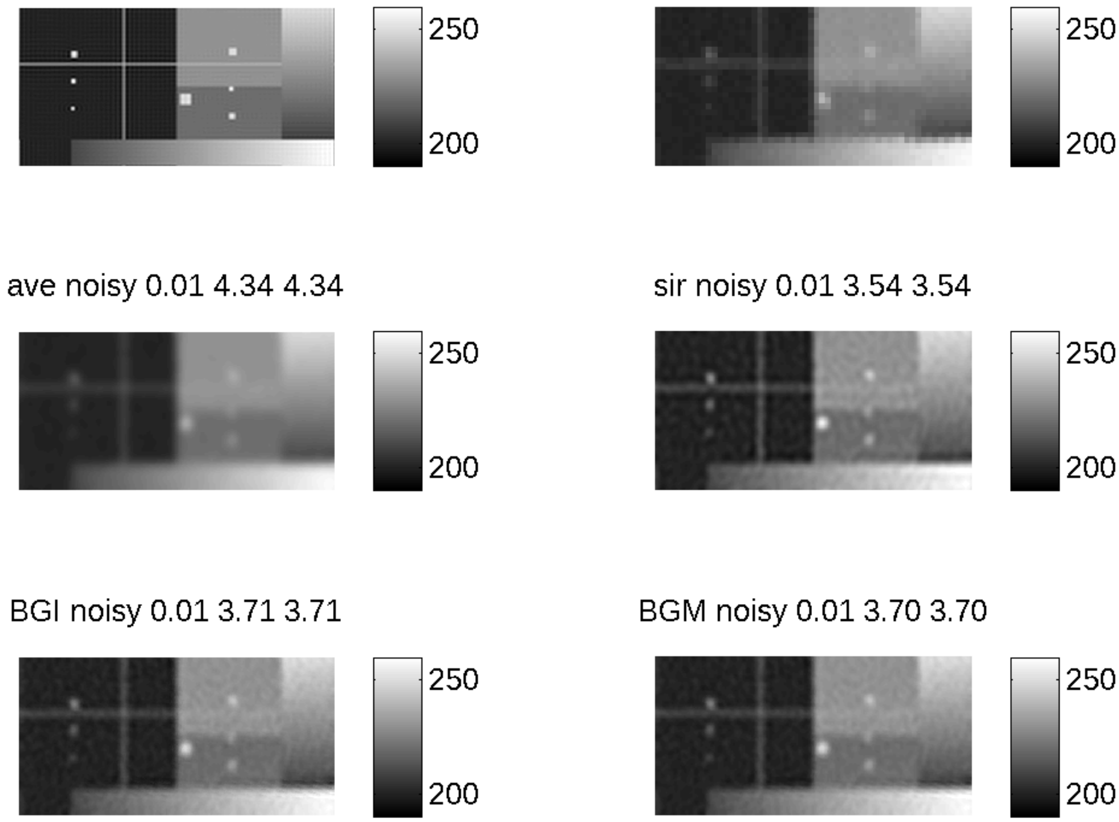

Figure 26. Comparison of true, Non (Grd), Ave, SIR, and BGI images with γ'=0.45 and BGI with median filter for the 37 GHz channel with N_s=3. Note the reduction in RMS error in BGI after median filtering.

As has been noted, BGI requires at least an order of magnitude more CPU than SIR. For larger values of N_s it can be several orders of magnitude more computation time; hence the desire for small values of N_s. The choice of gamma does not affect the computation, but changing the antenna gain cutoff from -9 dB to larger values can reduce the number of local measurements included in the matrix inversion, and thus the required CPU time. This is not considered here.

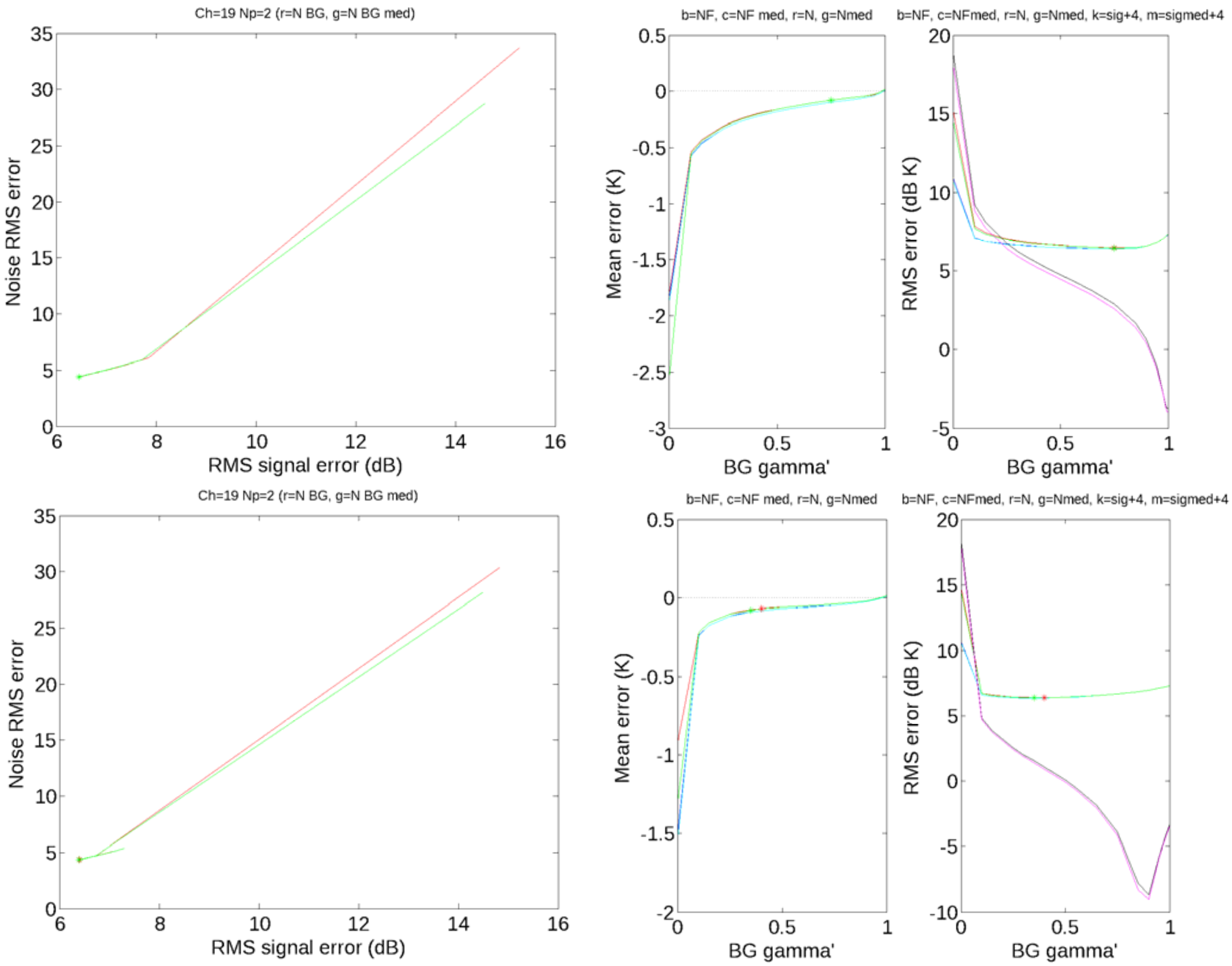

Figure 27. RMS noise power versus RMS signal error for 19 GHz, dual-pass, BGI image error versus gamma for (top) N_s=2, (bottom) N_s=3.

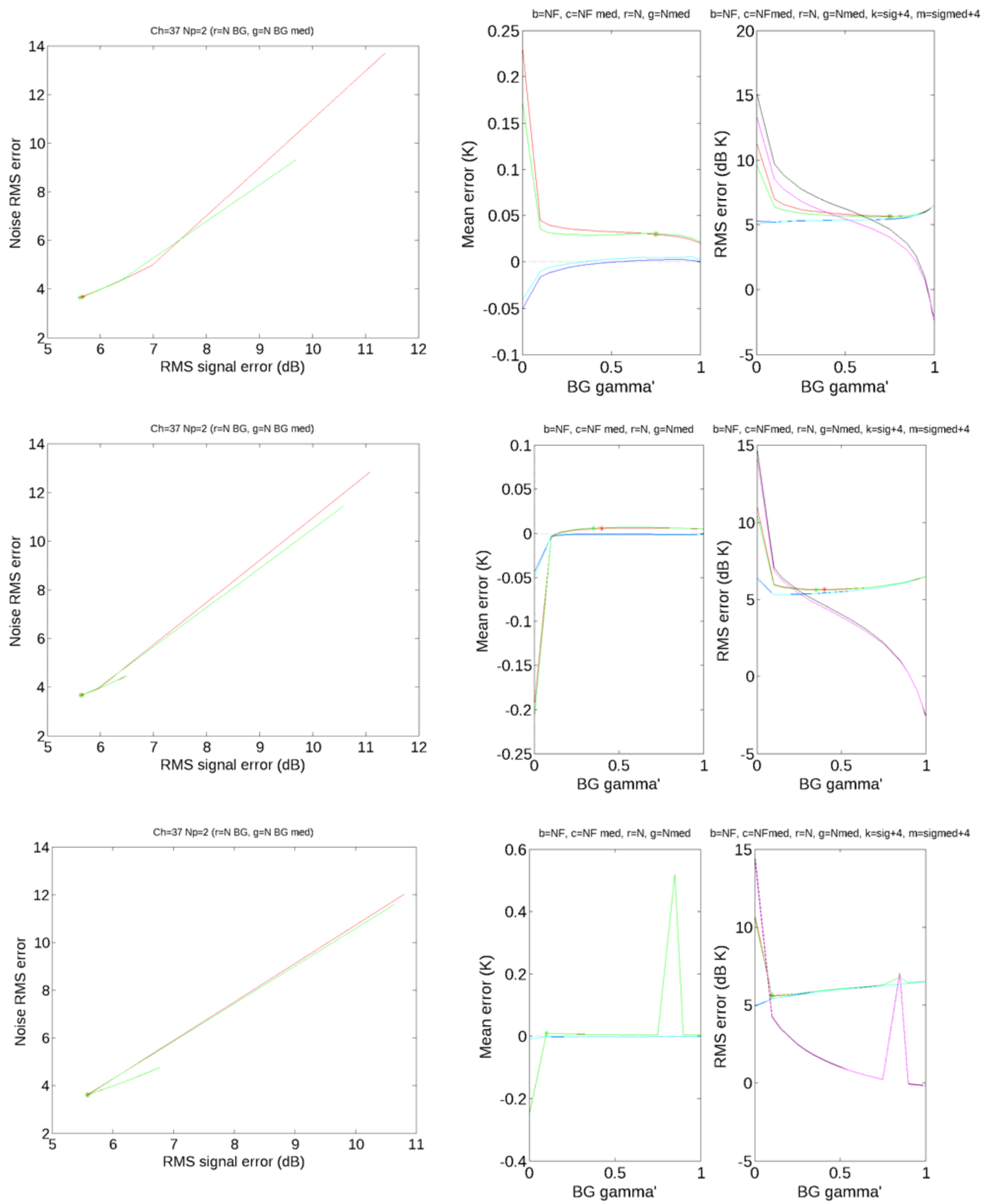

Figure 28. RMS noise power versus RMS signal error for 37 GHz, dual-pass, BGI image error versus gamma for (top) (middle) N_s=3, (bottom) N_s=4. Computational noise produces the spike observed in the lower right panel.

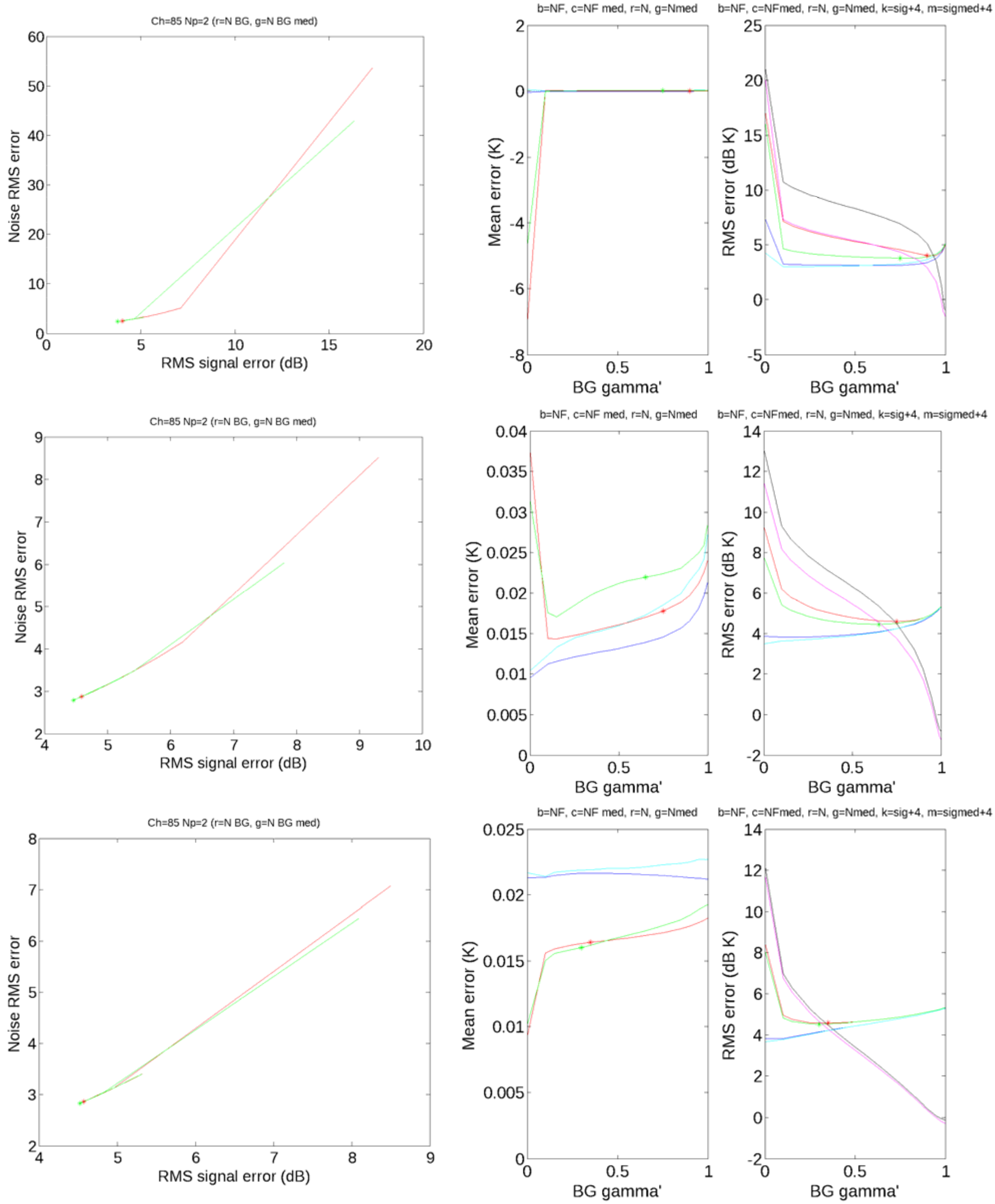

Figure 29. RMS noise power versus RMS signal error for 85 GHz, dual-pass, BGI image error versus gamma for (top) N_s=2, (middle) N_s=3, (bottom) N_s=4.

3.1 BGI Gamma and Pixel Sizes Considerations

We find that BGI provides better spatial resolution than conventionally gridded (NON) products, and similar performance to SIR. However, it requires much more computation. To minimize the computation, we recommend a smaller value of N_s for BGI images than the SIR recommendations. Based on the simulation results the recommended pixel size and BGI tuning parameter for each channel are given in Table 7.

Table 7: Recommend SSM/I BGI processing parameters by channel.

Channel	GRD pixel size	Pixel scale factor N_s and grid size P_s	BGI $g=\gamma/\pi$
19H	25 km	(2) 6.250 km	0.85
19V	25 km	(2) 6.250 km	0.85
22	25 km	(2) 6.250 km	0.85
37H	25 km	(2) 6.250 km	0.85
37V	25 km	(2) 6.250 km	0.85
85H	25 km	(3) 3.125 km	0.85
85V	25 km	(3) 3.125 km	0.85

4 Reconstruction Sensitivity to Inaccuracy in the Description of the MRF

In this section we study the sensitivity of the reconstruction results to errors in the description of the MRF. It has been previously noted that the MRF for some sensors is not known well. Even for those for which it is known well, there are uncertainties (errors) in the description of the MRF. This leads to the question, how sensitive is the reconstruction to the accuracy of the MRF?

In pursuing this question we note that we are interested only in the partial reconstruction case, e.g., when only a relatively small number of SIR iterations are performed. We expect the general conclusions to be similar for any partial reconstruction algorithm such as BGI.

We perform an experimental study in which simulated measurements of a synthetic scene are generated using the full MRF previously described. Then, different (erroneous) MRF descriptions are used in the reconstruction process. The results from the correct description and the erroneous descriptions are then compared. In the following, the same measurements from the previous simulations in the two-pass, Ns=3 case are used. Each channel is processed separately. We assume the true MRF is the two-dimensional Gaussian MRF previously described.

Eight different MRFs are created according to the following and used for generating images. These cases were arbitrarily chosen, but span a wide range of possible MRF errors. We note that while in some cases changing the number of SIR iterations can improve the error statistics, for this study the number of SIR iterations is fixed at 20 for all cases.

MRF used for reconstruction (see Fig. 30)

Case 1: "True". The MRF used for reconstruction is identical to that used for simulating the noisy measurements.

Case 2: "-3dB Binary". The MRF used for reconstruction is set to unity for the true MRF greater than or equal to one-half the peak MRF value (-3 dB of the peak). Thus, the MRF is a smaller elliptical "rect"-type response.

Case 3: "-6dB Binary". The MRF used for reconstruction is set to unity for the true MRF greater than or equal to one-quarter the peak MRF value (-6 dB of the peak). Thus, the MRF is a slightly larger elliptical "rect"-type response than for case 2.

Case 4: "Binary". The MRF used for reconstruction is set to unity for the true MRF greater than -30 dB of the peak MRF value. Thus, the MRF is an excessively large elliptical "rect"-type response.

Case 5: "Truncated 3dB". The MRF used for reconstruction is set to zero for the true MRF less than to one-half the peak MRF value (-3 dB of the peak), and is the same for values larger than the threshold. Thus, the MRF is a small, rounded ellipse.

Case 6: "Truncated 6dB". The MRF used for reconstruction is set to zero for the true MRF less than to one-quarter the peak MRF value (-6 dB of the peak), and is the same for values larger than the threshold. Thus, the MRF is a medium-sized, rounded ellipse.

Case 7: "Squared". The MRF used for reconstruction is set to be the square of the true MRF. Since the true MRF values are all less than or equal to one, squaring the MRF has the effect of making it more steep.

Case 8: "Square root". The MRF used for reconstruction is set to be the square root of the true MRF. Since the true MRF values are all less than or equal to one, squaring the MRF has the effect of flattening the response.

All the reconstruction MRFs are normalized to sum to one in the reconstruction processing.

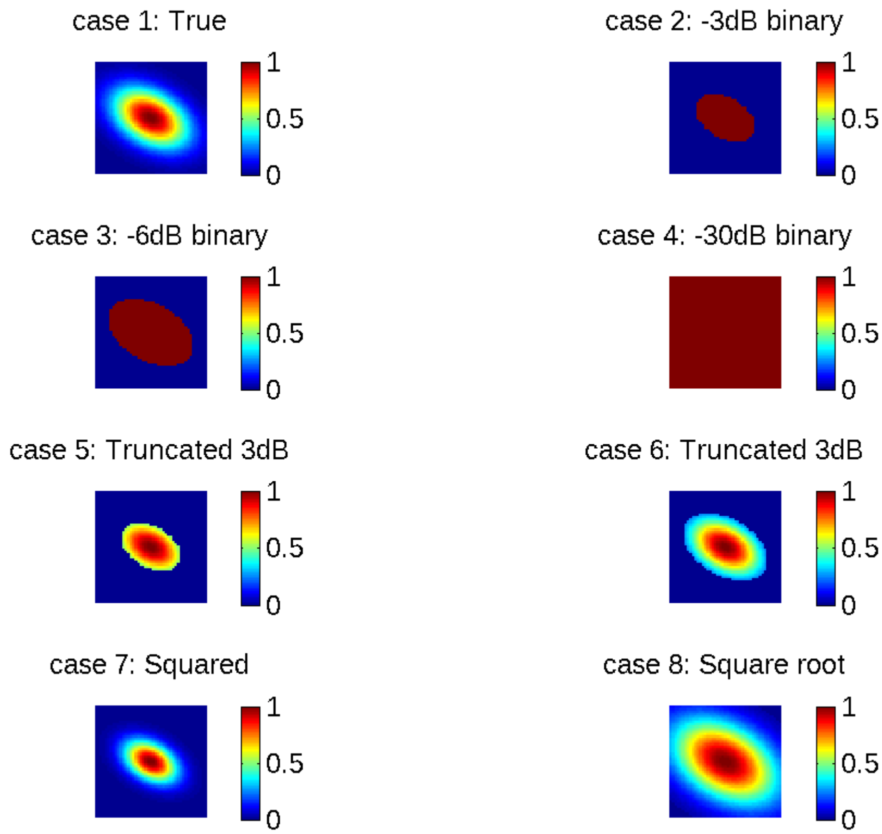

Figure 30. Images of the original and modified measurement response functions used in the simulation. Cases 2-4 are binary (0 or 1) with case 4 completely filling the enclosing square. Though not all are realistic, these particular cases were selected to span a large range of "errors" in the description of the MRF.

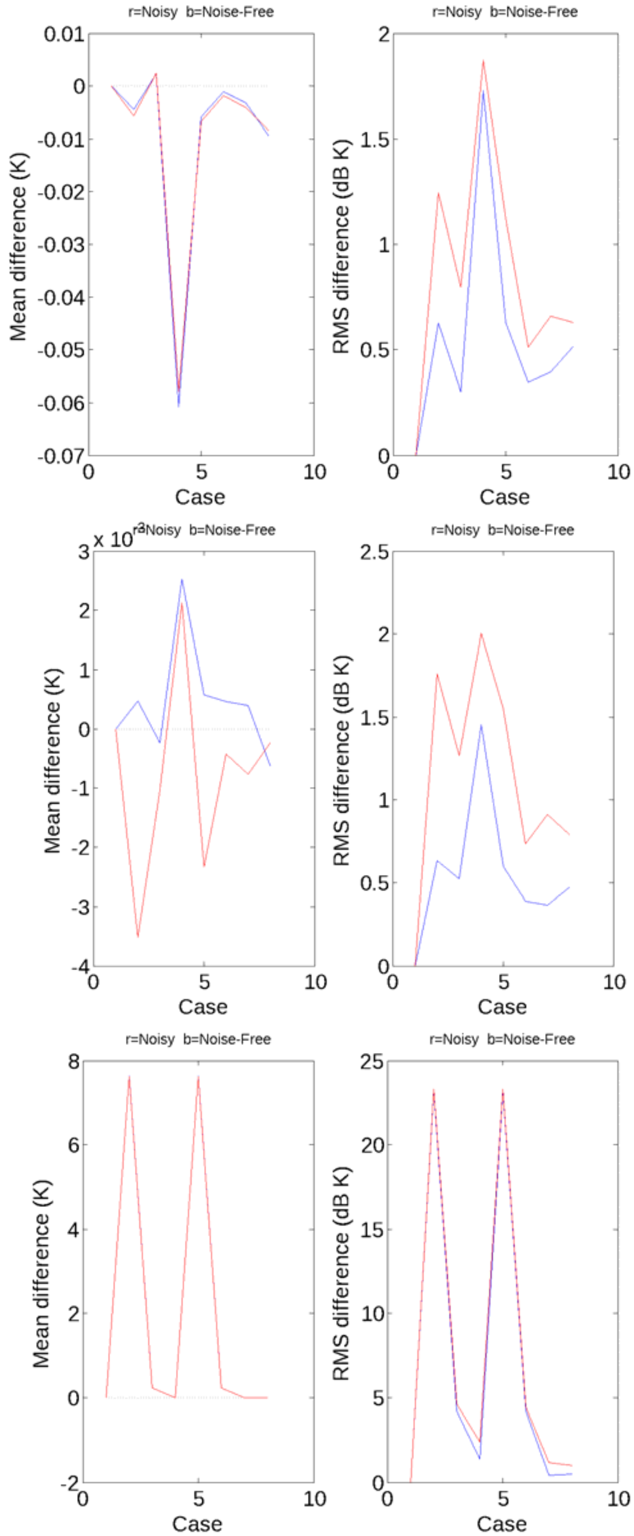

Figure 31. (left column) mean and (right column) RMS differences between the image reconstructed using the true (case 1) and erroneous (cases 2-8) MRF for the (top row) 19 GHz, (middle row) 37 GHz, and (bottom row) 85 GHz channels for Ns=3.

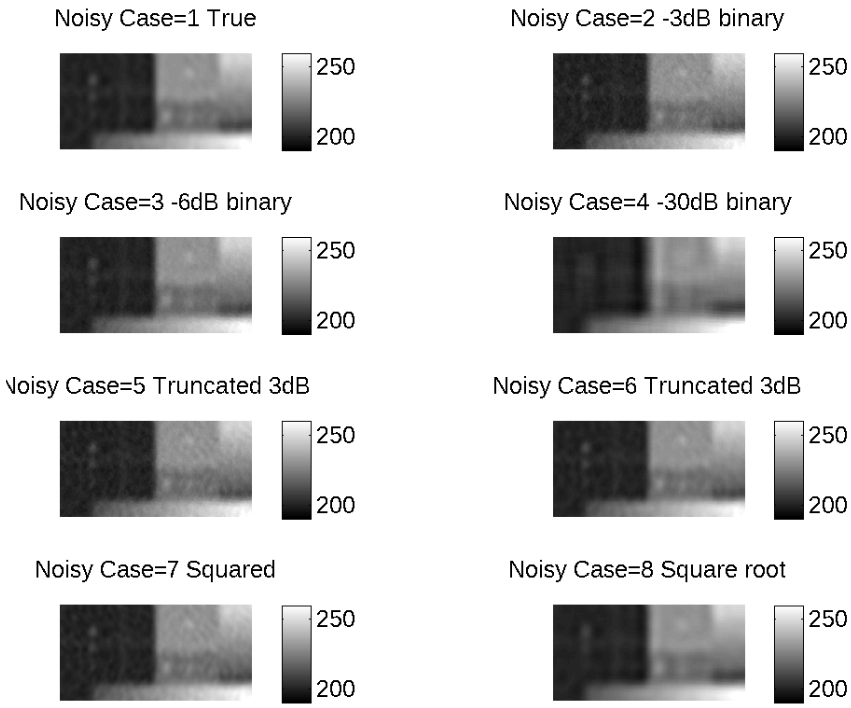

Figure 32. Images for each partial reconstruction case for 19 GHz.

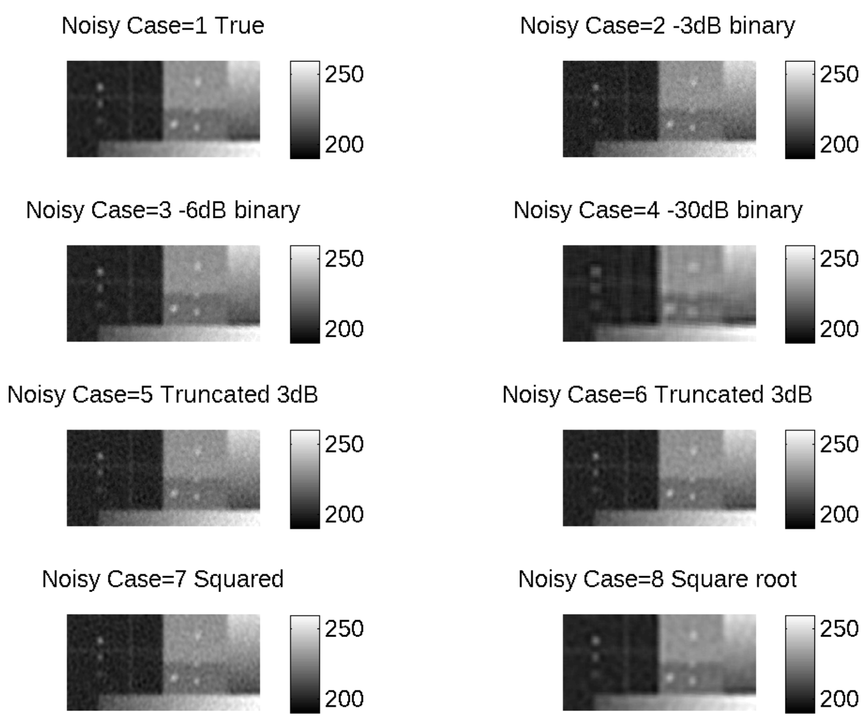

Figure 33. Images for each partial reconstruction case for 37 GHz.

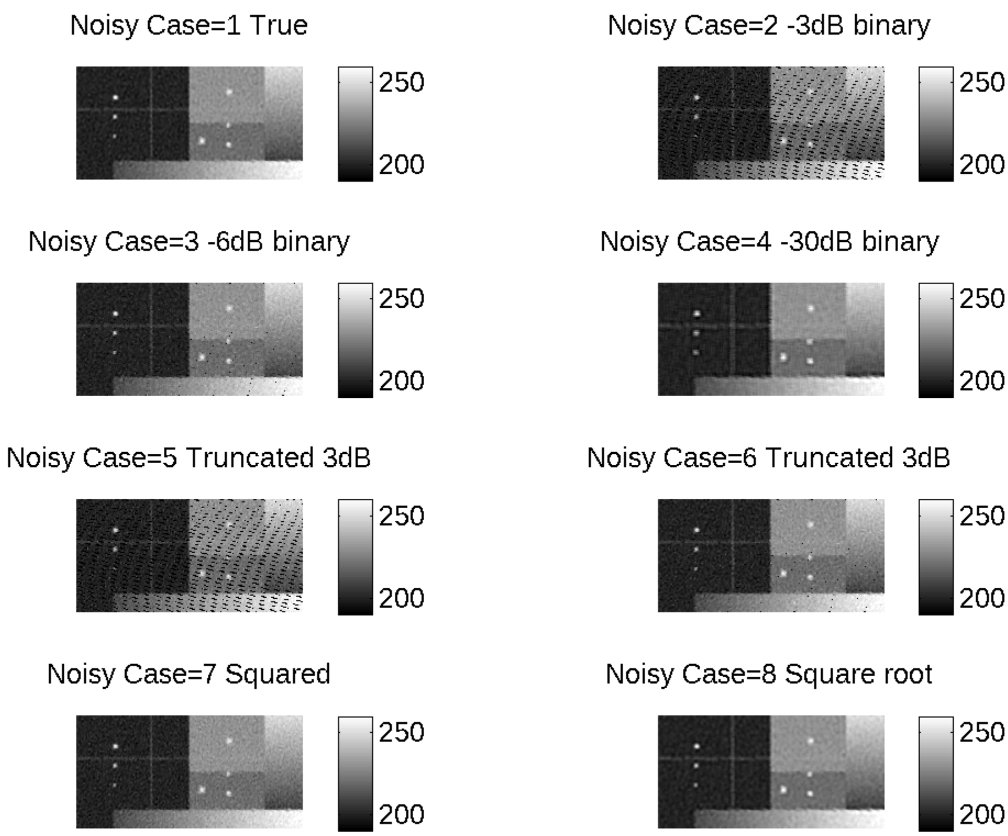

Figure 34. Images for each partial reconstruction case for the 85 GHz channel.

Figure 31 summarizes the mean and RMS differences between the image reconstructed with the true MRF (case 1) and the erroneous MRF (cases 2-8) for each channel. Corresponding images are shown in Figs. 32-34. Note from Figure 31 that the mean error is essentially zero for all cases. The RMS and standard deviations are thus essentially the same. The RMS error is the smallest when the true MRF is used, and is larger for the erroneous cases. However, the RMS error is generally not much larger for most cases, even when the MRF used for retrieval is very different than the true. The errors are the largest when the MRF used for retrieval is spatially much smaller than it should be, i.e., as evident in cases 2 and 5 at 85 GHz. The 6 dB cases, and the square and square root cases, have much smaller error. It is likely that errors in the description of the MRF will have only small rolloff errors, for which cases 7 and 8 (square and square root) represent worst cases.

These results suggest that so long as the assumed MRF is close, the RMS error is not particularly sensitive to the MRF used for reconstruction. To further explore this, we consider the family of erroneous MRFs defined by compute the fractional power of the true MRF, i.e. the MRF used for reconstruction *R'(x,y)* is computed from the true MRF *R(x,y)* using

$$R'(x, y) = R^r(x, y)$$

where $0<r<3$. (The square root and squared MRF used previously are particular examples with $r=0.5$ and $r=2$.) As r is varied in the range 0.25 to 3, the 3 dB footprint changes, and the response pattern rolloff characteristics change. Figure 35 plots the total noisy RMS error versus r for this case. Two curves are shown. One is for a fixed number of iterations (20 in this case). The other is the RMS error resulting when selecting the number of SIR iterations that minimized the total RMS error. This is the optimum number of SIR iterations. Note that in all cases the variation in the RMS error is small, and the difference between the fixed and the optimum number of iterations is very small.

These simulation results reveal that using the correct MRF for reconstruction minimizes the error, but modest distortions in the MRF used in the reconstruction have very limited impact on the accuracy of the reconstruction results. The variation in total RMS error with MRF distortion is small for all channels and cases. Thus the results of the reconstruction are not particularly sensitive to the accuracy of the MRF, and we can successfully use approximate MRF models. This is a fortunate result since it means that precise antenna pattern descriptions are not required for generating high resolution brightness temperature images. All that is needed is that the descriptions be reasonably accurate.

So why can we get away with imprecise descriptions of the antenna pattern in the reconstruction process? Since the noise is amplified as the signal is enhanced, there is a tradeoff between the signal reconstruction error and the noise increase. This trade off leads us to truncate the iterative reconstruction process before it is complete, i.e. we only do partial reconstruction and do not fully reconstruct the signal. The simulations show that partial reconstruction can tolerate modest errors in the MRF description and still yield reasonable estimates of the desired signal. Not shown is that when the erroneous MRF is used to attempt to fully reconstruct the signal, the final signal is distorted compared to the signal resulting from the correct MRF description.

The relative insensitivity of the partially reconstructed image to the MRF description suggests that we can get away with less than perfect descriptions of the MRF. This is critical since, as noted earlier in Section 2.1, precise descriptions are not available for all sensors. We can thus use a simple two-dimensional Gaussian model discussed in Section 2.1.

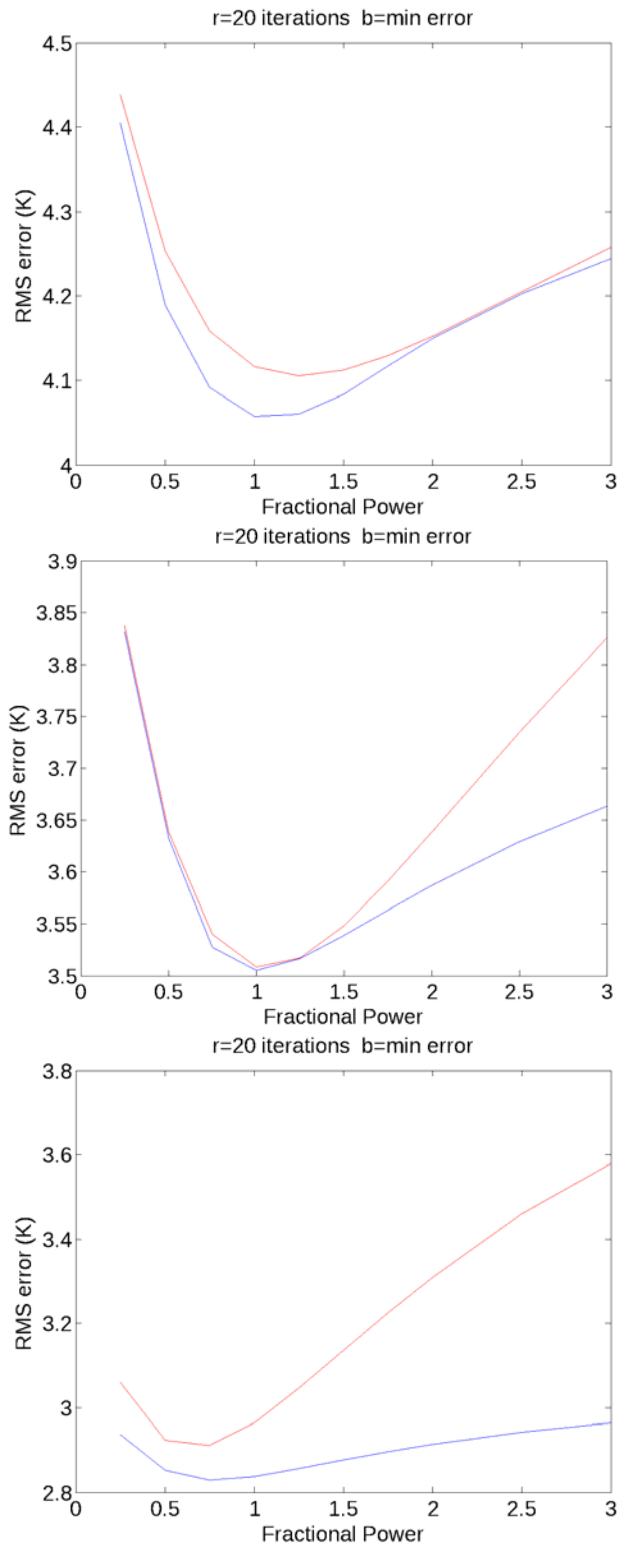

Figure 35. Plots of the noisy total RMS error versus fractional power *r* for (top row) 19 GHz, (middle row) 37 GHz, and (bottom row) 85 GHz. The red curve is the error for 20 iterations. The blue is the RMS error that minimized the total RMS versus SIR iteration number, and thus is a lower bound.

5 References

Armstrong, R., K. Knowles, M. Brodzik, and M. A. Hardman. 1994, updated 2014. DMSP SSM/I-SSMIS Pathfinder Daily EASE-Grid Brightness Temperatures. Version 1. Boulder, Colorado USA: NASA DAAC at the National Snow and Ice Data Center.

Backus, G.E., and J. F. Gilbert, 1967. Numerical applications of a formalism for geophysical inverse problems, *Geophys. J. R. Astron. Soc.*, vol. 13, pp. 247–276.

Backus, G.E., and J. F. Gilbert, 1968. Resolving power of gross Earth data*, Geophys. J. R. Astron. Soc.*, vol. 16, pp. 169–205.

Brodzik, M. J. and D.G. Long. 2014. "Calibrated Passive Microwave Daily EASE-Grid 2.0 Brightness Temperature ESDR (CETB): Algorithm Theoretical Basis Document," National Snow and Ice Data Center (NSIDC) publication [Online] Available at: (TBD link needed).

Brodzik, M. J. and K. W. Knowles. 2002. "EASE-Grid: a versatile set of equal-area projections and grids" in M. Goodchild (Ed.) Discrete Global Grids. National Center for Geographic Information & Analysis, Santa Barbara, CA: USA. [Online] Available at: http://www.ncgia.ucsb.edu/globalgrids-book/ease_grid/.

Brodzik, M. J., B. Billingsley, T. Haran, B. Raup, M. H. Savoie. 2012. EASE-Grid 2.0: Incremental but significant improvements for Earth-Gridded data sets. *ISPRS International Journal of Geo-Information*, 1(1):32-45. [Online] Available at: http://www.mdpi.com/2220-9964/1/1/32/.

Caccin, B., C. Roberti, P. Russo, and A. Smaldone, 1992. The Backus–Gilbert inversion method and the processing of sampled data, *IEEE Trans. Signal Processing*, vol. 40, pp. 2823–2825.

Chakraborty, P., A. Misra, T. Misra, and S.S. Rana, 2008. Brightness Temperature Reconstruction Using BGI, *IEEE Trans. Geosci. Remote Sensing*, vol. 46, no. 6, pp. 1768–1773.

Early D.S., and D.G. Long, 2001. Image Reconstruction and Enhanced Resolution Imaging from Irregular Samples, *IEEE Transactions on Geoscience and Remote Sensing*, Vol. 39, No. 2, pp. 291-302.

Farrar, M.R., and E. A. Smith, 1992. Spatial resolution enhancement of terrestrial features using deconvolved SSM/I brightness temperatures, *IEEE Trans. Geosci. Remote Sensing*, vol. 30, pp. 349–355.

Galantowicz, J. F., A. W. England. 1991. The Michigan Earth Grid: Description, Registration Method for SSM/I Data, and Derivative Map Projections. Radiation Laboratory, Department of Electrical Engineering and Computer Science, Technical Report 027396-2-T. University of Michigan, Ann Arbor, Michigan USA.

Galantowicz, J. F. 1995. *Microwave Radiometry of Snow-Covered Grasslands for the Estimation of Land-Atmosphere Energy and Moisture Fluxes*. PhD Thesis, Department of Electrical Engineering and Computer Science and Department of Atmospheric, Oceanic, and Space Sciences. University of Michigan, Ann Arbor, Michigan USA.

Long, D.G., and D.L. Daum, 1998. Spatial Resolution Enhancement of SSM/I Data," *IEEE Transactions on Geoscience and Remote Sensing*, Vol. 36, No. 2, pp. 407-417.

Long, D.G., P. Hardin, and P. Whiting, 1993. Resolution Enhancement of Spaceborne Scatterometer Data, *IEEE Transactions on Geoscience and Remote Sensing*, Vol. 31, No. 3, pp. 700-715.

Poe, G.A., 1990. Optimum interpolation of imaging microwave radiometer data, *IEEE Trans. Geosci. Remote Sensing*, vol. 28, pp. 800–810.

Robinson, W.D., C. Kummerow, and W. S. Olson, 1992. A technique for enhancing and matching the resolution of microwave measurements from the SSM/I instrument, *IEEE Trans. Geosci. Remote Sensing*, vol. 30, pp. 419–429.

Sethmann, R., B. A. Burns, and G. C. Heygster, 1994. Spatial resolution improvement of SSM/I data with image restoration techniques, *IEEE Trans. Geosci. Remote Sensing*, vol. 32, pp. 1144-1151.

Stephens, P.J., and A.S. Jones. 2002. A computationally efficient discrete Backus-Gilbert footprint-matching algorithm. *IEEE Trans. Geosci. Remote Sensing*, vol. 40, no. 8, pp. 1865-1878.

Stogryn, A., 1978. Estimates of brightness temperatures from scanning radiometer data, *IEEE Trans. Antennas Propagat.,* vol. AP-26, pp. 720–726.

Swift, C.T., M.A. Goodberlet, and S. C. Reising, 2006. Antenna Pattern Synthesis and Deconvolution of Microwave Radiometer Imaging Data, *IEEE MicroRad 2006*, pp. 216-221.